J. Fluid Mech. (2006), *vol.* 551, *pp.* 63–92.
doi:10.1017/S002211200500827X Printed in the United Kingdom

Evolving eddy structures in oscillatory Stokes flows in domains with sharp corners

By M. BRANICKI AND H. K. MOFFATT

Department of Applied Mathematics and Theoretical Physics, University of Cambridge, Wilberforce Road, Cambridge CB3 0WA, UK
mb388@damtp.cam.ac.uk, hkm2@damtp.cam.ac.uk

(Received 25 February and in revised form 10 August 2005)

Stokes flow of a viscous fluid in a cylindrical container driven by time-periodic forcing, either at the boundary or through oscillation of the cylinder about an axis parallel to its generators, is considered. The behaviour is governed by a dimensionless frequency parameter η and by the geometry of the cylinder cross-section. Various cross-sections (square, rhombus, and sector of a circle) are first treated by either finite-difference or analytic techniques and typical transitions of streamline topology during flow reversals are identified. Attention is then focused on the asymptotic behaviour near any sharp corner on the boundary. For small η, a regular perturbation expansion reveals the manner in which local flow reversal proceeds during each half-cycle of the flow. The behaviour depends on the corner angle, and different regimes are identified for both types of forcing. For example, for an oscillating square domain, eddies grow symmetrically from each corner and participate in the subsequent flow reversal in the interior. For large η, the corner eddies merge into Stokes-type boundary layers which drive the interior flow-reversal process. In general, the local corner analysis provides a key to an understanding of the global flow evolution.

1. Introduction

Stokes flow of an incompressible fluid in a finite domain $\mathscr{D}$ is generally thought to be 'quasi-static', i.e. instantaneously determined throughout $\mathscr{D}$ by the velocity distribution on its boundary $\partial\mathscr{D}$. For such a flow, if the boundary is instantaneously at rest, then the fluid is everywhere at rest irrespective of the previous history of the motion. Thus, for example, if a tangential motion that is sinusoidal in time is imposed on part or all of $\partial\mathscr{D}$, then the interior flow will have a constant streamline pattern, the intensity varying sinusoidally at each point, a reversal of the flow direction occurring at each instant when the boundary is momentarily at rest.

This quasi-static description is clearly inadequate, since in all practical circumstances for a fluid of finite viscosity, it takes a finite time for vorticity to diffuse from the boundary to the fluid interior. In particular, if the boundary is brought to rest at any instant, a residual motion remains within the fluid at that instant. In a time-periodic flow driven by sinusoidal boundary motion, this residual motion at the instants when the boundary is at rest provides the key to understanding how the above flow reversals occur in practice.

The situation is amenable to analysis, which turns out to be particularly revealing, when $\mathscr{D}$ has one or more sharp corners on its boundary, and the flow is two-dimensional. The generic steady Stokes flow in the neighbourhood of such corners has been long understood (Moffatt 1964): if the angle of the corner is less than a

critical value (approximately 146°), and the flow is driven by an input remote from the corner, then the flow is characterized by a sequence of self-similar eddies of alternating sense (clockwise and anticlockwise) and rapidly decreasing intensity as the corner is approached. If the remote input (whether by boundary motion or otherwise) is now supposed to be sinusoidal in time, then the quasi-static description would imply an instantaneous and simultaneous reversal of all the eddies in this sequence at each moment of input reversal. This is scarcely credible, and a more realistic description must be sought through consideration of the residual flow effect. We shall find that this consideration yields a time-periodic flow in which topological transitions occur in such a way as to allow for flow reversals without ever passing through a state of complete rest.

We shall focus on two prototypical situations. The first (the 'oscillating lid problem') is that for which the flow is driven by an oscillatory tangential motion of part of the boundary (which can be thought of as a 'sleeve' or a 'lid' depending on circumstances); this is the situation studied by Shankar, Kidambi & Hariharan (2003) for the case of a rectangular cavity with oscillating lid, in which the importance of the 'residual flow' phenomenon described above was recognized. The second (the 'oscillating cylinder problem') is that in which the cylinder $\mathscr{D}$ is subjected to torsional oscillations about an axis parallel to its generators; in this case, it is the flow relative to the cylinder (i.e. the departure from a rigid-body motion) that is of interest. It is of historical interest to note that this type of problem was first conceived by Stokes (1843) in a study of the potential flow inside a rectangular parallelepiped, subjected to an arbitrary translation and rotation. We shall refer further to this paper in § 5 below.

These two prototype problems may both be approached within a common framework, as described in § 2 below, although significant differences will emerge later. For given geometry, and in the limit of low Reynolds number, the only surviving parameter is a dimensionless frequency parameter η. In § 3, we discuss general characteristics of the flow reversal and show examples of the process for various geometries of the boundary. In §§ 4 and 5, we seek to understand the origin of these flow reversals through consideration of the local behaviour near any sharp corner. For low η, this may be treated by a regular perturbation expansion (§ 4), while for large η (§ 5) a matching between 'core flow' and a Stokes-type boundary layer is required. In each case, the analysis reveals the essential flow-reversal mechanisms.† Finally, in the Appendix, we present details of the analytical method as applied in § 3 for the oscillating cylinder problem based on truncated eigenfunction expansions.

2. Mathematical formulation

Consider first the two-dimensional, unsteady flow of a viscous incompressible fluid contained in a cylinder of cross-section $\mathscr{D}$ which is subjected to torsional oscillatory motion with angular velocity $\boldsymbol{\Omega} = \Omega(t)\boldsymbol{k}$ about an axis parallel to its generators. We shall refer to this as the 'oscillating-cylinder problem'. The cross-section $\mathscr{D}$ is arbitrary; it may have one or more sharp corners on its boundary, and it need not be simply connected. In a (non-inertial) frame of reference fixed relative to the cylinder, the flow is governed by the Navier–Stokes equation in the form

$$\left.\begin{aligned} &\frac{\partial \boldsymbol{u}}{\partial t} + \boldsymbol{u}\cdot\nabla\boldsymbol{u} = -\frac{\nabla p}{\rho} + \nu\nabla^2\boldsymbol{u} - 2\boldsymbol{\Omega}\wedge\boldsymbol{u} - \boldsymbol{\Omega}\wedge(\boldsymbol{\Omega}\wedge\boldsymbol{r}) - \dot{\boldsymbol{\Omega}}\wedge\boldsymbol{r}, \\ &\nabla\cdot\boldsymbol{u} = 0, \end{aligned}\right\} \tag{2.1}$$

† These are most vividly exposed by computer animations, which are available as a supplement to the online version of this paper.

with the no-slip boundary condition $\boldsymbol{u}=0$ on $\partial\mathscr{D}$. The terms $-2\boldsymbol{\Omega}\wedge\boldsymbol{u}-\boldsymbol{\Omega}\wedge(\boldsymbol{\Omega}\wedge\boldsymbol{r})$ are (for two-dimensional flow) irrotational and may be absorbed in the pressure term; the Poincaré force $-\dot{\boldsymbol{\Omega}}\wedge\boldsymbol{r}$ is however rotational, and drives a flow relative to the cylinder. With streamfunction $\psi(x,y,t)$ such that $u=\partial\psi/\partial y$, $v=-\partial\psi/\partial x$, the vorticity is $\boldsymbol{\omega}=-\nabla^2\psi\,\boldsymbol{k}$, and ψ satisfies

$$\frac{\partial\nabla^2\psi}{\partial t}+\frac{\partial(\nabla^2\psi,\psi)}{\partial(x,y)}-\nu\nabla^4\psi=2\dot{\Omega},\quad \psi=\frac{\partial\psi}{\partial n}=0\ \text{ on }\ \partial\mathscr{D}, \tag{2.2}$$

where the Poincaré term $2\dot{\Omega}$ evidently provides a uniform rate of production of vorticity within the domain.

Let L be the characteristic scale of the cross-section $\mathscr{D}$ and let $\hat{\omega}$, $\hat{\Omega}$ be respectively the characteristic frequency and amplitude of the torsional oscillations. If we then non-dimensionalize lengths with L, time with $\hat{\omega}^{-1}$, and velocities with $\hat{U}(=2\hat{\Omega}L)$, (2.2) takes the non-dimensional form

$$\eta\frac{\partial\nabla^2\psi}{\partial t}+Re\frac{\partial(\nabla^2\psi,\psi)}{\partial(x,y)}-\nabla^4\psi=\eta\,\dot{\Omega},\quad \psi=\frac{\partial\psi}{\partial n}=0\ \text{ on }\ \partial\mathscr{D}, \tag{2.3}$$

where $Re=\hat{U}L/\nu$ is the Reynolds number and $\eta=\hat{\omega}L^2/\nu$. These two parameters can be varied independently by changing $\hat{U}$ and $\hat{\omega}$.

A related problem that we shall refer to as the 'oscillating-lid problem' concerns the flow inside the cylindrical domain $\mathscr{D}$ generated by a prescribed oscillatory tangential velocity distribution $\mathscr{U}$ on the boundary with some characteristic frequency $\hat{\omega}$ and amplitude $\hat{U}$. The Navier–Stokes equation governing this flow can be written

$$\left.\begin{aligned}&\frac{\partial\boldsymbol{u}}{\partial t}+\boldsymbol{u}\cdot\nabla\boldsymbol{u}=-\frac{\nabla p}{\rho}+\nu\nabla^2\boldsymbol{u},\\&\nabla\cdot\boldsymbol{u}=0,\\&\boldsymbol{u}\cdot\boldsymbol{n}=0,\quad \boldsymbol{u}\cdot\boldsymbol{t}=\mathscr{U}(s,t)\quad\text{on}\quad\partial\mathscr{D},\end{aligned}\right\} \tag{2.4}$$

where $\boldsymbol{n}$, $\boldsymbol{t}$ are the unit normal and tangent vectors on $\partial\mathscr{D}$; s is a variable along the boundary (e.g. arc-length). We may again non-dimensionalize using L, $\hat{\omega}^{-1}$, and $\hat{U}$ as scales of length, time and velocity, and the problem (2.4) reduces to

$$\eta\frac{\partial\nabla^2\psi}{\partial t}+Re\frac{\partial(\nabla^2\psi,\psi)}{\partial(x,y)}-\nabla^4\psi=0,\qquad \psi=0,\ \ \frac{\partial\psi}{\partial n}=\mathscr{U}(s,t)\quad\text{on}\ \ \partial\mathscr{D}. \tag{2.5}$$

The governing equation and boundary conditions for both prototype problems (2.5) and (2.3) can be compacted in the form

$$\left.\begin{aligned}&\eta\frac{\partial\nabla^2\psi}{\partial t}+Re\frac{\partial(\nabla^2\psi,\psi)}{\partial(x,y)}-\nabla^4\psi=\Lambda\,\eta\,\dot{\Omega}(t),\\&\psi=0,\quad \partial\psi/\partial n=(1-\Lambda)\mathscr{U}(s,t)\quad\text{on}\ \ \partial\mathscr{D},\end{aligned}\right\} \tag{2.6}$$

where $\Lambda=1$ for the oscillating-cylinder problem and $\Lambda=0$ for the oscillating-lid problem.

We now adopt the conventional Stokes approximation $Re\ll1$, which allows us to drop the nonlinear convective acceleration term in (2.6). We further suppose that $Re\ll\eta$ so that it is consistent to retain the local acceleration term $\eta\partial\nabla^2\psi/\partial t$, which plays an important part in the subsequent analysis. These two conditions may be combined in the form

$$\hat{U}/\hat{\omega}\ll L\ll\nu/\hat{U}, \tag{2.7}$$

and evidently

$$\hat{U}^2/\nu\hat{\omega} = Re(Re/\eta) \ll 1. \tag{2.8}$$

Having linearized the problem, we may analyse the flow due to a single Fourier mode of the forcing. In complex notation, with real parts understood, we set $\Omega = \mathrm{e}^{\mathrm{i}t}$ in the oscillating-cylinder problem, or $\mathscr{U} = u(s)\mathrm{e}^{\mathrm{i}t}$ in the oscillating-lid problem, and we seek solutions of the form $\psi = \hat{\psi}(x, y)\,\mathrm{e}^{\mathrm{i}t}$†. Thus, based on (2.6), $\hat{\psi}(x, y)$ satisfies

$$\left.\begin{aligned} &\nabla^2\hat{\psi} - (\mathrm{i}\eta)^{-1}\nabla^4\hat{\psi} = \Lambda, \\ &\psi = 0, \quad \partial\psi/\partial n = (1-\Lambda)u(s) \quad \text{on } \partial\mathscr{D}. \end{aligned}\right\} \tag{2.9}$$

We note that Shankar *et al.* (2003) have studied this system for the oscillating-lid problem ($\Lambda = 0$) in a rectangular geometry. It is crucial to note that, as recognized by Shankar *et al.*, the amplitude $\hat{\psi} = \hat{\psi}_r + \mathrm{i}\hat{\psi}_\mathrm{i}$ is in general complex so that the final time-dependent streamfunction has the general form

$$\Psi(x, y, t) = \mathrm{Re}[\hat{\psi}(x, y)\,\mathrm{e}^{\mathrm{i}t}] = \hat{\psi}_r \cos t - \hat{\psi}_\mathrm{i} \sin t. \tag{2.10}$$

Hence, as long as $\hat{\psi}$ is complex and $\hat{\psi}_r \neq c\hat{\psi}_i$ with c real, the streamfunction Ψ given by (2.10) represents an oscillatory flow which is not quasi-steady. This manifestation of fluid inertia is a direct consequence of retaining the unsteady term in the Navier–Stokes equation whereby the flow adjusts itself to the oscillations of the forcing in a non-trivial fashion. In the following sections, we shall focus on the nature of the periodic flow reversals, first from a global, then from a local perspective.

3. Global aspects of flow reversal in a closed domain

In the two situations specified in the previous section (oscillating cylinder and oscillating lid), the flow reversal is initiated at the boundary $\partial\mathscr{D}$ and subsequently proceeds inwards. In order to understand this mechanism, we first focus on topological changes in the evolving flow structure which occur in the interior and in the 'low-η' regime (the description in this section is qualitatively correct up to $\eta \sim 200$; the 'high-η' regime, when oscillatory boundary layers play an important part in the flow reversal, is discussed in § 5). In subsequent sections, we shall analyse different mechanisms for the onset of flow reversal based on local solutions near sharp corners on the boundary. It turns out that the final stage of the flow reversal, which takes place in the interior, is qualitatively independent of the actual onset mechanism and is determined primarily by symmetries of the domain.

The problem of finding an analytical solution of the amplitude equation (2.9) in an arbitrary domain is prohibitive. It is however possible to obtain an approximate analytical solution to (2.9) in a rectangular geometry based on the so-called superposition method (see the Appendix). This yields an exact solution in the form of an infinite series whose coefficients satisfy an infinite system of algebraic equations. Here we simply present some results obtained by this method for a square domain. We then present a number of numerical solutions of (2.9), obtained by standard finite-difference techniques, for a variety of other geometries, and we indicate certain common characteristics of the flow reversal process which are independent of the domain geometry.

† By doing so, we obviously exclude from consideration any transient phenomena associated with the initial stage of the evolution if the fluid is accelerated from rest.

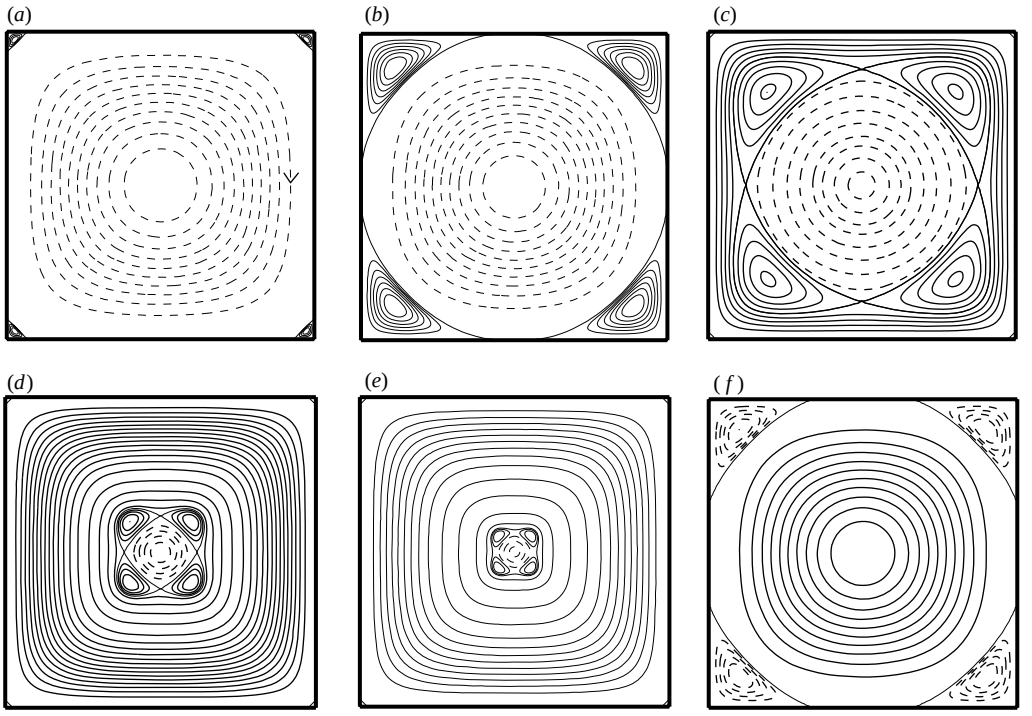

FIGURE 1. Flow reversal in an oscillating square domain in the low-η regime for $\eta = 100$; for smaller values of η the reversal process is virtually the same but occurs on a shorter time scale. (High-η reversal is shown in figure 14.) Snapshots of a sequence of streamline patterns in the non-inertial frame oscillating with the cylinder with (non-dimensional) angular velocity $\Omega(t) = \cos t$: (*a*) $t = 0$, (*b*) $t = 0.61$ – primary corner eddies, rotating in opposite sense to the central eddy, grow inwards, (*c*) $t = 0.94$ – dividing streamlines detach from the walls and create a heteroclinic connection, (*d*) $t = 1.38$, (*e*) $t = 1.41$ – the heteroclinic connection shrinks and eventually annihilates the central eddy, (*f*) $t = \pi + 0.55$ – the next flow reversal progresses in a similar way.

3.1. *Flow reversal in a square*

The process of flow reversal inside an oscillating cylinder of square cross-section is shown in figure 1 for $\eta = 100$. The sequence of snapshots captures the topological evolution of the streamline pattern during a flow reversal. A reversal starts roughly when the angular velocity of the oscillating cylinder ($\Omega = \cos t$) is extremal, i.e. at $t = t_n = n\pi$, when the forcing term in (2.9) vanishes. Four corner eddies, which counter-rotate relative to the central eddy, emerge from the corners and progress diagonally towards the centre. The points of attachment of the dividing streamlines move along the boundary and eventually merge to form a heteroclinic streamline connecting four saddle points. This heteroclinic structure shrinks in time and the central eddy is eventually annihilated in a heteroclinic bifurcation (with four-fold symmetry, corresponding to the symmetry of the domain) at the centre. This process is repeated periodically. As will be clarified in § 4 below, the time scale of this flow reversal decreases with η and the whole process occurs within a short time interval centred on each $t_n = n\pi$ when η is small. In the limit $\eta = 0$, the process becomes quasi-steady and the reversals are instantaneous.

As mentioned previously, flow reversal inside a rectangular cavity driven by an oscillating lid has been described by Shankar *et al.* (2003). We note that the

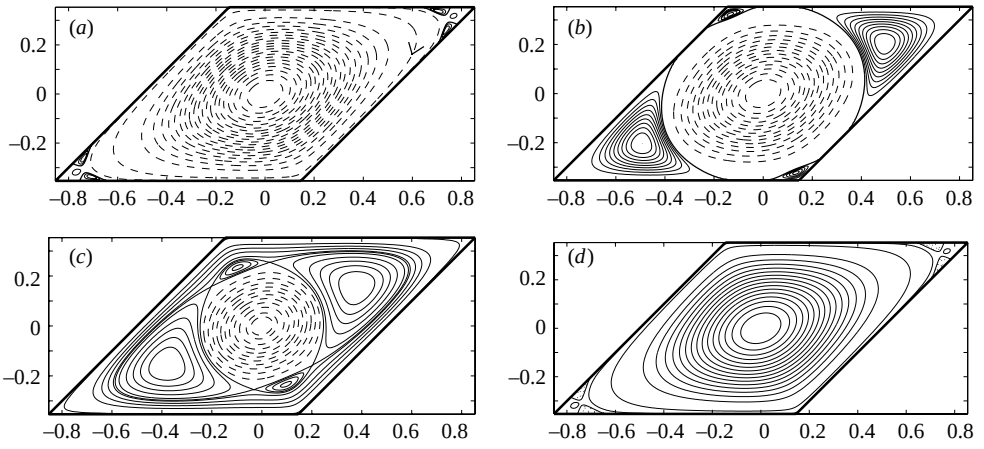

FIGURE 2. Flow reversal inside an oscillating cylinder with rhomboidal cross-section in the low-η regime for $\eta = 100$ (compare with figures 1, 3). Sequence of instantaneous streamline patterns of Ψ shown in the non-inertial frame oscillating with the cylinder for (*a*) $t = -0.0065$, (*b*) $t = 0.47$, (*c*) $t = 0.72$, (*d*) $t = \pi - 0.0065$. As for the square geometry, a heteroclinic connection of four saddles annihilates the counter-rotating central eddy. Note that pairs of side wall eddies appear in the acute-angle corners and that eddies in the obtuse-angle corners appear much later. See the following sections for explanation of this phenomenon.

superposition method described in the Appendix provides an alternative method of deriving an approximate solution to this problem, and we have found this to be in broad confirmation of Shankar *et al.*'s results.

3.2. *Flow reversal in other geometries*

We present here some further examples of the process of flow reversal based on numerical solution of (2.9) in non-rectangular domains, using a second-order finite-difference scheme. As before, the flow evolution is obtained by substituting the computed amplitude function $\hat{\psi}$ into Ψ, given by (2.10); and figures 2–4 present sequences of streamline patterns $\Psi = \text{const}$.

Figure 2 shows the time-periodic evolution in a rhomboidal domain of interior angles $2\alpha_1 = 45°$, $2\alpha_2 = 135°$, with $\eta = 100$. Note that at the onset of the flow reversal, in contrast to the case of the square domain, pairs of sidewall eddies now emerge from the walls in the acute-angle corners and there are at first no visible eddies present in the obtuse-angle corners. The sidewall pairs of eddies, which counter-rotate relative to the central eddy, later merge into expanding corner eddies and the two dividing streamlines created in the merger process start moving in opposite directions. The dividing streamline which moves into the interior of the domain is later involved in a heteroclinic connection of four saddle points. The final stage of the flow reversal is qualitatively similar to that for the square domain, the heteroclinic structure shrinking to annihilate the original central eddy. It is evident again that the flow reversal process is initiated by the emergence of the corner eddies; this process will be examined by detailed local analysis in § 4.

Consider now two examples of evolution inside a sector of a circle of angle $2\alpha = 60°$, again with $\eta = 100$. Figure 3 shows the oscillating-cylinder case when the whole contour is subjected to torsional oscillations. At the onset of the flow reversal, a pair of sidewall eddies again emerges from the walls in the acute-angle corner and two simple eddies emerge from the remaining corners. The sidewall eddies eventually

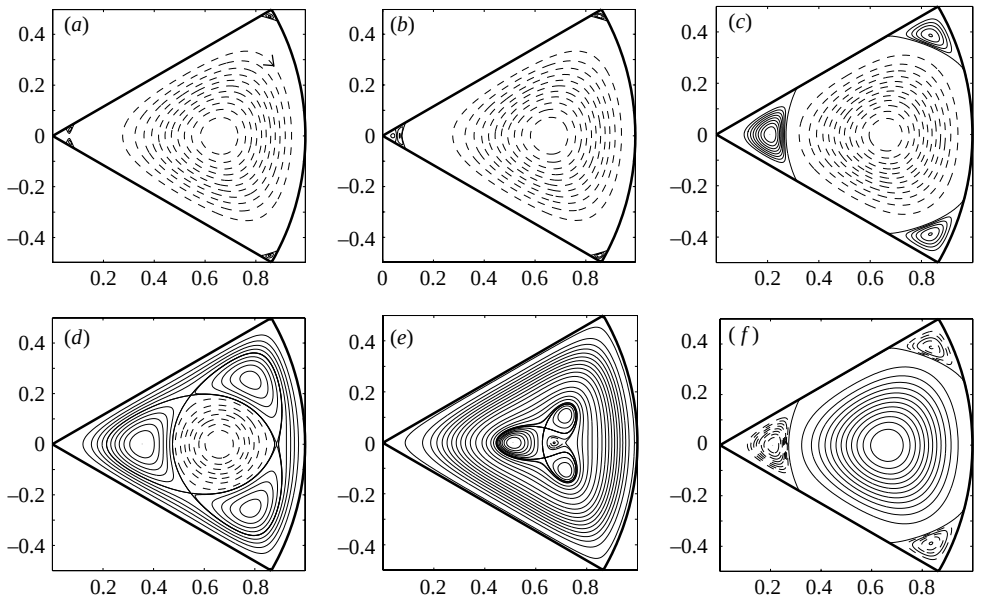

FIGURE 3. Oscillating-cylinder problem: flow reversal inside sector of a circle (60°) in the low-η regime for $\eta = 100$. Sequence of instantaneous streamline patterns of the time-periodic streamfunction Ψ (2.10) shown in the non-inertial frame oscillating with the cylinder for (*a*) $t = -0.086$, (*b*) $t = -0.08$, (*c*) $t = 0.35$, (*d*) $t = 0.69$, (*e*) $t = 0.9$, (*f*) $\pi + 0.35$. The mechanism is similar to that in the square (see figure 1) although this time one heteroclinic connection is created (involving two saddles) and one homoclinic connection (see (*e*)).

merge into a single expanding corner eddy and pairs of separation points of the dividing streamlines move towards each other along the boundary. As in the previous cases, the corner eddies counter-rotate relative to the central eddy and occupy an increasingly large area of the domain. Due to a lesser degree of symmetry, there appears in this case a heteroclinic connection of just two saddle points, and a homoclinic streamline whose saddle point moves along the bisector of the angle. The final stage of the flow reversal involves a sequence of global bifurcations, the homoclinic connection playing a dominant role; but as in the previous cases, the net effect is that the whole structure shrinks towards the centre in such a way as to annihilate the original central eddy.

Figure 4 shows the oscillating-lid case, when the curved part of the boundary (the 'lid') is rotated about the centre with sinusoidal angular velocity. The flow reversal begins when the lid velocity is about to reverse. Two eddies, counter-rotating relative to the central eddy, emerge from the corners adjacent to the lid (figure 4*c*) and later merge into a single expanding eddy located under the lid (figure 4*d*). At approximately the same time, the corner eddy opposite the moving lid expands inwards, and when the separation points meet on the boundary a heteroclinic connection of two saddle points is formed. The original central eddy eventually disappears in a heteroclinic bifurcation at the centre.

Based on these examples, we may conjecture that the final stage of the flow reversal process is quite generally realized by a sequence of global bifurcations in the instantaneous streamline pattern of the flow. In the process, the central eddy disappears in a global bifurcation involving one or more saddles created when the

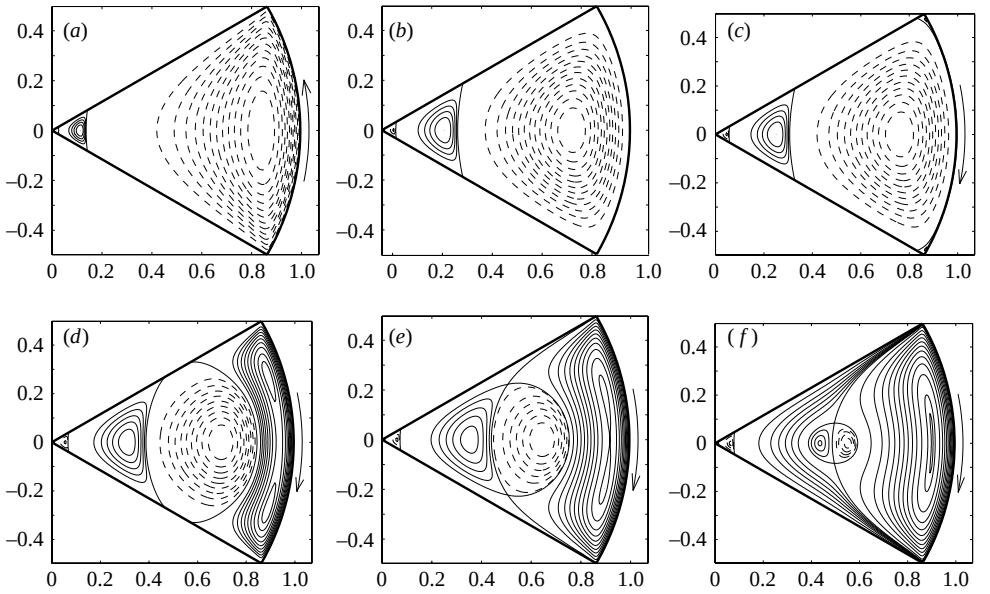

FIGURE 4. Oscillating-lid problem: flow reversal inside sector of a circle (60°) for $\eta = 100$. Sequence of instantaneous streamline patterns of the time-periodic streamfunction Ψ (2.10) shown for (*a*) $t = 0$, (*b*) $t = \pi/2$, (*c*) $t = 1.58$, (*d*) $t = 1.95$, (*e*) $t = 2.1$, (*f*) $t = 2.25$.

dividing streamlines detach from the boundary. In highly symmetric geometries, the original central eddy is annihilated by a single heteroclinic structure.

4. Perturbation analysis for small η and local solutions

In this section, we shall examine the low-frequency limit $\eta \ll 1$, and we shall for the most part focus on the behaviour near any sharp corners on the boundary. Actually, in a local analysis, the length scale of the domain L becomes irrelevant, and the corner analysis is valid at distances r from the corner satisfying the inequalities (replacing (2.7))

$$\hat{U}/\hat{\omega} \ll r \ll \nu/\hat{U}. \tag{4.1}$$

We expand $\hat{\psi}$ in a power series

$$\hat{\psi} = \hat{\psi}_0 + \eta\,\hat{\psi}_1 + \eta^2\,\hat{\psi}_2 + \eta^3\,\hat{\psi}_3 + \ldots, \tag{4.2}$$

substitute in (2.9) and equate terms with the same power of η; this yields the following equations for the oscillating-lid and oscillating-cylinder problems:

$$\left.\begin{array}{ll} \text{Oscillating lid} & \text{Oscillating cylinder} \\ \nabla^4\hat{\psi}_0 = 0 & \hat{\psi}_0 \equiv 0 \\ \nabla^4\hat{\psi}_1 = \mathrm{i}\nabla^2\hat{\psi}_0, & \nabla^4\hat{\psi}_1 = -\mathrm{i} \\ \nabla^4\hat{\psi}_2 = \mathrm{i}\nabla^2\hat{\psi}_1 & \nabla^4\hat{\psi}_2 = \mathrm{i}\nabla^2\hat{\psi}_1, \\ \quad\vdots & \quad\vdots \\ \nabla^4\hat{\psi}_n = \mathrm{i}\nabla^2\hat{\psi}_{n-1}, & \nabla^4\hat{\psi}_n = \mathrm{i}\nabla^2\hat{\psi}_{n-1}. \end{array}\right\} \tag{4.3}$$

For the oscillating lid, this sequence begins with the homogeneous biharmonic equation which has been extensively studied in the context of steady Stokes flow. For the oscillating-cylinder problem, $\hat{\psi}_0 \equiv 0$ indicates that at the zeroth order the fluid oscillates with the cylinder as a rigid body, i.e. the flow is identically zero in the adopted non-inertial cylinder frame.

Note that for real forcing the successive amplitude functions $\hat{\psi}_k$, $(k = 0, 1, 2, \ldots)$ are alternately real and pure imaginary. Consequently, the streamfunction Ψ takes the form

$$\Psi = \mathrm{Re}[\hat{\psi}\, \mathrm{e}^{\mathrm{i}t}] = \psi_0 \cos t - \eta\, \hat{\psi}_1 \sin t + \cdots + \eta^{2k}\, \hat{\psi}_{2k} \cos t - \eta^{2k+1} \hat{\psi}_{2k+1} \sin t + \ldots. \tag{4.4}$$

In both cases the flow is quasi-steady at leading order and the (weak) inertial effects due to the unsteady term are accounted for at the next order of approximation. This higher-order term ($O(\eta)$ in the oscillating-lid case and $O(\eta^2)$ in the oscillating-cylinder case) becomes important near times t_n when the trigonometric function ($\cos t$ or $\sin t$ respectively) multiplying the leading-order term is close to zero. Consequently, for most of the cycle the streamline topology is that of the leading-order term. However, in each small time interval

$$\Delta t_n = \left(t_n - \tfrac{1}{2}\Delta t, t_n + \tfrac{1}{2}\Delta t\right), \quad \Delta t = O(\eta), \tag{4.5}$$

the higher-order correction is comparable in magnitude with the leading-order term. In each such time interval

$$\Psi(x, y, t) \approx (-1)^n \eta^2 [\hat{\psi}_2 - \tau \hat{\psi}_1], \tag{4.6}$$

for the oscillating-cylinder case, and

$$\Psi(x, y, t) \approx (-1)^{n+1} \eta [\hat{\psi}_1 - \tau \hat{\psi}_0], \tag{4.7}$$

for the oscillating-lid case, where $\tau = \eta t$. This approximation is sufficient to describe the reversal process as the scaled time τ runs through zero from large negative to large positive values. In both situations the time scale of the flow reversal is $O(\eta)$.

4.1. *Time-periodic flow near a corner*

We now investigate the asymptotic time-periodic flow structure near any sharp corner on the boundary. As before, we assume that the flow is generated by oscillating some part of the boundary (oscillating lid) or by oscillating the whole contour (oscillating cylinder) and solve a related problem in a wedge. We may later constrain the solution by imposing additional 'remote' boundary conditions. It is convenient here to consider the two problems separately:

4.1.1. *Oscillating lid*

There are two kinds of corner flow in this case, that near a corner remote from the moving lid, and that near a 'lid corner' where the boundary velocity is discontinuous.

(i) *Remote corner*. Based on (4.3) the zero-order solution for the oscillating-lid problem requires solution of the biharmonic problem in the wedge

$$\nabla^4 \hat{\psi}_0(r, \theta) = 0, \qquad \hat{\psi}_0 = \frac{\partial \hat{\psi}_0}{\partial \theta} = 0 \quad \text{on} \quad \theta = \pm\alpha. \tag{4.8}$$

The general solution of (4.8) (Moffatt 1964) takes the form

$$\hat{\psi}_0 = \sum_{n=1}^{\infty} A_n f_n(\theta) r^{\lambda_n} = \sum_{n=1}^{\infty} (a_n \,\mathrm{Re}[f_n(\theta) r^{\lambda_n}] + b_n \mathrm{Im}[f_n(\theta) r^{\lambda_n}]), \tag{4.9}$$

where

$$f_n(\theta) = \cos(\lambda_n - 2)\alpha\, \cos\lambda_n\theta - \cos\lambda_n\alpha\, \cos(\lambda_n - 2)\theta, \tag{4.10}$$

and the (complex) constants $A_n(=a_n - \mathrm{i}b_n)$ are determined (in principle) by the details of the remote forcing. The eigenvalues are complex-conjugate pairs $(\lambda_n, \bar{\lambda}_n)$, and may be ordered so that

$$1 < \mathrm{Re}[\lambda_1] < \mathrm{Re}[\lambda_2] < \cdots < \mathrm{Re}[\lambda_n] < \ldots. \tag{4.11}$$

They are the roots (with $\mathrm{Re}[\lambda] > 1$) of the transcendental equation

$$\sin 2(\lambda - 1)\alpha = -(\lambda - 1)\sin 2\alpha. \tag{4.12}$$

At the first order, we seek the solution of the inhomogeneous biharmonic equation

$$\nabla^4\hat{\psi}_1 = \chi, \quad \hat{\psi}_1 = \frac{\partial\hat{\psi}_1}{\partial\theta} = 0, \quad \text{on} \quad \theta = \pm\alpha, \tag{4.13}$$

with

$$\chi(r,\theta) = \mathrm{i}\nabla^2\hat{\psi}_0 = 4\mathrm{i}\sum_{n=1}^{\infty} A_n(1-\lambda_n)\cos\lambda_n\alpha\, \cos(\lambda_n - 2)\theta\, r^{\lambda_n - 2}. \tag{4.14}$$

This takes the form

$$\hat{\psi}_1 = \mathrm{i}\sum_{n=1}^{\infty}(C_n f_n(\theta) r^{\lambda_n} + A_n h_n(\theta) r^{\lambda_n+2}) = \mathrm{i}\sum_{n=1}^{\infty}(c_n \mathrm{Re}[f_n(\theta)r^{\lambda_n}] + d_n \mathrm{Im}[f_n(\theta)r^{\lambda_n}])$$
$$+ \mathrm{i}\sum_{n=1}^{\infty}(a_n \mathrm{Re}[h_n(\theta)r^{\lambda_n+2}] + b_n \mathrm{Im}[h_n(\theta)r^{\lambda_n+2}]), \tag{4.15}$$

where f_n is given by (4.10) and the functions

$$h_n(\theta) = \frac{\cos\lambda_n\alpha}{8\lambda_n}\left[\frac{\lambda_n \sin 4\alpha + 2\sin 2\lambda_n\alpha}{(\lambda_n+1)\sin 2\alpha + \sin 2(\lambda_n+1)\alpha}\cos\lambda_n\theta - \cos(\lambda_n - 2)\theta\right] \tag{4.16}$$

arise from the 'particular solution' forced by the term χ in (4.13). Since as we have noted, for real forcing, $\hat{\psi}_0$ is real, and $\hat{\psi}_1$ is pure imaginary, the coefficients a_n, b_n, c_n, d_n are all real and the real time-dependent streamfunction is therefore given by

$$\Psi(x, y, t) = \mathrm{Re}[\hat{\psi}\mathrm{e}^{\mathrm{i}t}] = \hat{\psi}_0\cos t - \eta\,\hat{\psi}_1 \sin t + O(\eta^2). \tag{4.17}$$

Near $r = 0$, $\hat{\psi}_0$ and $\hat{\psi}_1$ are in general dominated by the terms with $n = 1$ which involve the lowest powers of r; thus

$$\left.\begin{aligned} \hat{\psi}_0 &\sim a_1 \mathrm{Re}[f_1(\theta)r^{\lambda_1}] + b_1 \mathrm{Im}[f_1(\theta)r^{\lambda_1}] \\ \hat{\psi}_1 &\sim \mathrm{i}c_1 \mathrm{Re}[f_1(\theta)r^{\lambda_1}] + \mathrm{i}d_1 \mathrm{Im}[f_1(\theta)r^{\lambda_1}] \\ &\quad + \mathrm{i}a_1 \mathrm{Re}[h_1(\theta)r^{\lambda_1+2}] + \mathrm{i}b_1 \mathrm{Im}[h_1(\theta)r^{\lambda_1+2}] \end{aligned}\right\} \quad \text{as} \quad r \to 0. \tag{4.18}$$

For $2\alpha \lesssim 146.2^\circ$, $\mathrm{Im}[\lambda_1] \neq 0$, and both these streamfunctions exhibit the familiar phenomenon of infinitely oscillatory behaviour as $r \to 0$ (Moffatt 1964). For $2\alpha \gtrsim 146.2$, when λ_1 is real, there are no corner eddies in the structure of Ψ. Hence, we may conclude that, sufficiently near a sharp corner, there are two distinct regimes of corner angles (see figure 10*a*) below where the local time-periodic flow has different characteristics:

Regime I $(0 < 2\alpha \lesssim 146.2^\circ)$: there is an infinite sequence of (time-dependent) eddies in the streamline pattern of Ψ throughout the time-periodic evolution.

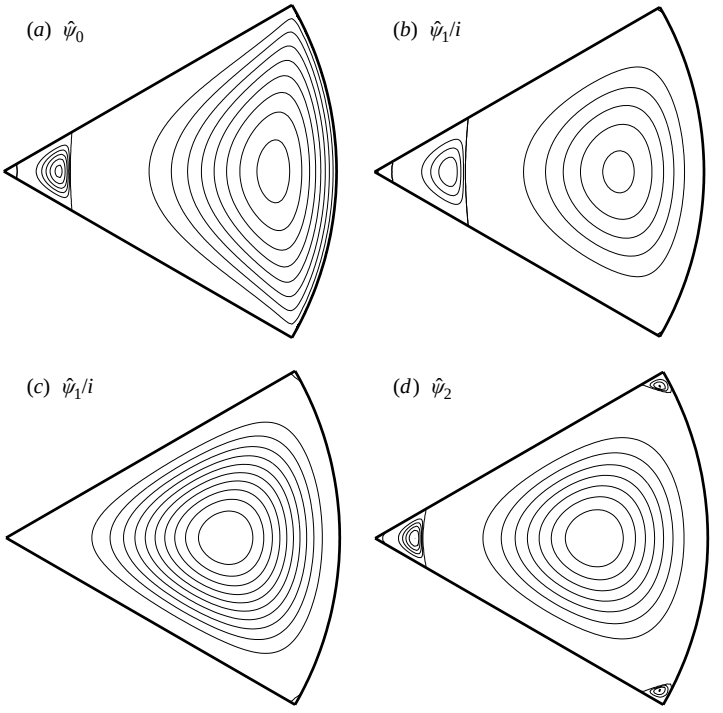

FIGURE 5. Structure of the functions $\hat{\psi}_0$ and $\hat{\psi}_1/\mathrm{i}$ in a corner closed by a circular arc $r=1$ on which the the boundary condition is satisfied by a least-squares collocation technique; (a, b) oscillating-lid problem; (c, d) oscillating-cylinder problem.

Regime II ($2\alpha \gtrsim 146.2$): There are no corner eddies during most of the periodic evolution, but during the flow reversal, there may be at most a single corner eddy resulting from the competing structures of $\hat{\psi}_0$ and $\hat{\psi}_1$. The dividing streamline is given by $\Psi = 0$ (as long as this connects to the walls).

In order to present some specific examples, we consider the situation when the flow is driven by an oscillating lid at position $r=1$. The coefficients a_n, b_n, c_n, d_n (or at any rate a finite number of them) may be determined using a collocation technique (cf. Shankar 1993). This involves truncation of the series in (4.9), (4.15) to the first N terms, choosing $M(>2N)$ discrete points on the boundary $r=1$, and determining $4N$ coefficients in such a way that the boundary conditions on $r=1$ are satisfied in a least-squares sense at these points. For corner angle $2\alpha = 60^\circ$ (regime I) and with $N=40$ and $M=200$, this procedure yields $a_1 \approx 0.1928$, $b_1 \approx 0.4056$, $c_1 \approx 0.001$, $d_1 \approx -0.0068$ (see figure 5a, b). A sequence of snapshots of the resulting time-periodic flow (given by (4.17)) is presented in figure 6 for $\eta = 0.1$. For this small value of η, the primary corner eddy, visible in figure 6(a), remains almost steady for most of the period. Then, in a very short time interval, it moves into the interior of the domain (its outermost dividing streamline ultimately participates in the heteroclinic connection discussed in the previous section). Simultaneously, another eddy, rotating in the opposite sense, emerges from the corner to take the place of the primary eddy. This eddy will also move into the interior after another half-period.

This behaviour is in a sense very beautiful! The infinite sequence of corner eddies present in a steady Stokes flow are inaccessible to observation (after the first two or three), because they decay so rapidly as the corner is approached. But when the flow

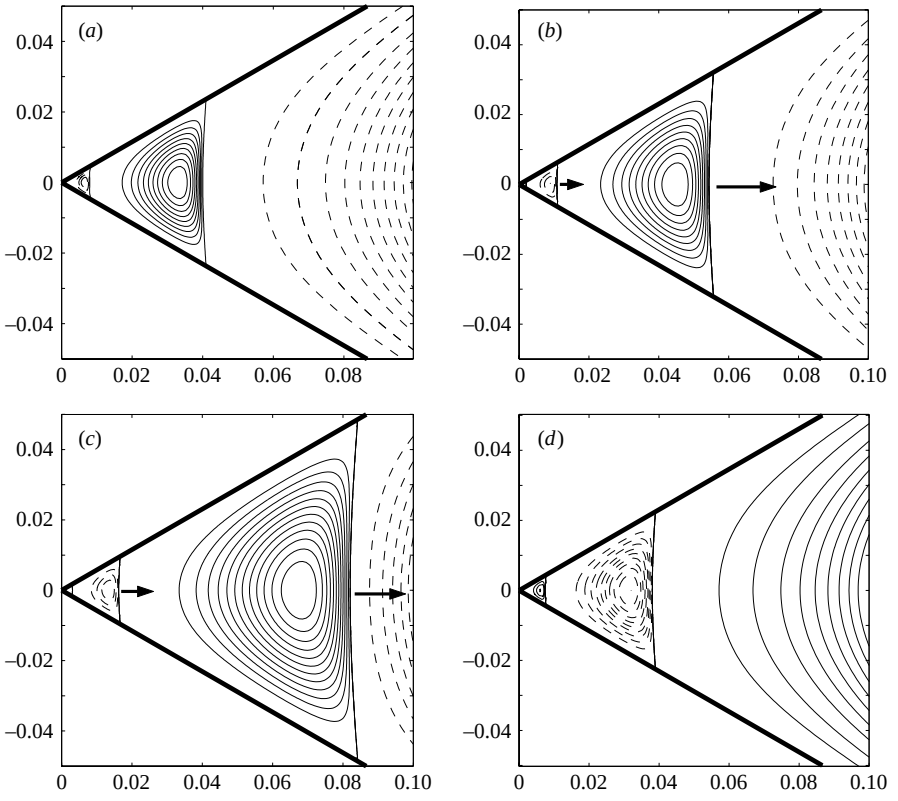

FIGURE 6. Time-periodic evolution of the infinite eddy structure, characteristic of regime I, near a 60° corner in a flow generated by an oscillating lid at $r=1$; $\eta=0.1$ in this example. The sequence of streamline patterns of Ψ (4.17) is shown during the short time interval within which the flow reverses: (*a*) $t=\pi/2-0.01$, (*b*) $t=\pi/2$, (*c*) $t=\pi/2+0.0011$, (*d*) $t=\pi/2+0.01$. The contours shown are not equidistant. The primary corner eddy which rotates in the opposite sense to the main body of the fluid emerges from the corner, and simultaneously, the secondary corner eddy replaces the primary one in the corner. Note that similar evolution takes place in regime III of the oscillating-cylinder problem (see figure 10).

is oscillatory, at low frequency, it is as if these eddies were being coaxed out of the corner one at a time, to participate in the successive flow-reversal processes in the central part of the fluid domain.

Turning now to regime II ($2\alpha \gtrsim 146.2$), there are two possible scenarios: there may be either a single eddy or no eddies generated during the flow reversal. Evolution involving a single eddy is shown in figure 7 where $2\alpha = 160°$ (so that $\mathrm{Im}[f_1(\theta)r^{\lambda_1}] \equiv 0$). Imposing the oscillating-lid conditions as before and using the least-squares technique yields in this case $a_1 \approx -1.0035$, $c_1 \approx 0.0155$ (the coefficients b_n and d_n do not enter). For most of the period there is no eddy in the corner, but a single dividing streamline $\Psi(x, y, t)=0$ emerges at some $t > \pi$. Finally, an example of evolution near a corner of reflex angle $2\alpha = 270°$, is shown in figure 8; here $a_1 \approx -0.7920$, $c_1 \approx 0.0151$. No corner eddies appear in this situation during the flow reversal.

(ii) *Lid corner*. In this case, the zeroth-order problem reduces to

$$\nabla^4\hat{\psi}_0(r,\theta)=0, \qquad \hat{\psi}_0(r,\pm\alpha)=0, \quad \frac{1}{r}\frac{\partial\hat{\psi}_0}{\partial\theta}\bigg|_{\theta=\alpha}=1, \quad \frac{1}{r}\frac{\partial\hat{\psi}_0}{\partial\theta}\bigg|_{\theta=-\alpha}=0, \tag{4.19}$$

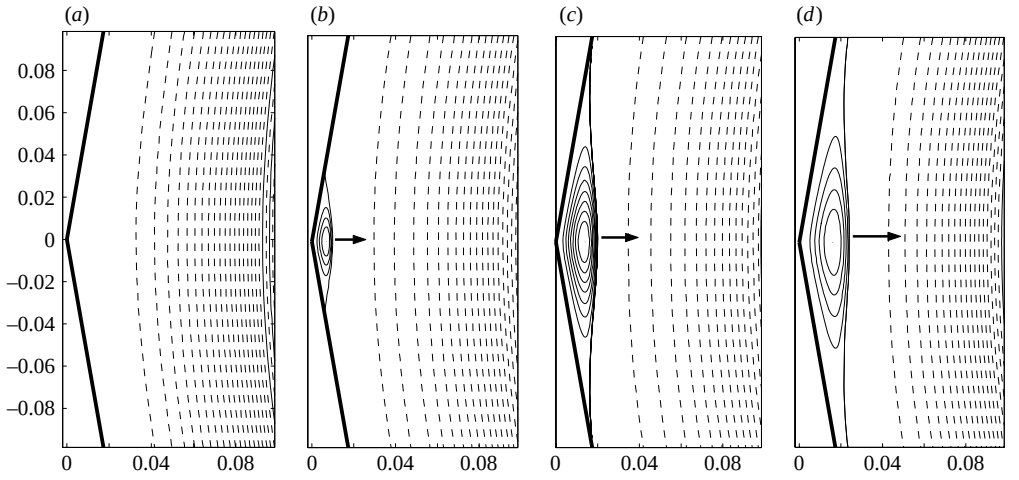

FIGURE 7. Emergence of a single eddy during the flow reversal in a 160° corner (regime II) in the oscillating lid flow; $\mathrm{Im}(\lambda_1)=0$ and there are no infinite eddy structures in the flow. Similar evolution takes place in regime IV of the oscillating-cylinder problem (see figure 10). Time sequence of instantaneous streamline patterns in a very short time interval when the flow reverses its direction. (*a*) $t=\pi/2$, (*b*) $t=\pi/2+0.00161$, (*c*) $t=\pi/2+0.00165$, (*d*) $t=\pi/2+0.001665$. The dividing streamline, determined by $\Psi(x, y, t)=0$, eventually detaches from the wall and becomes involved in a heteroclinic connection (not shown here).

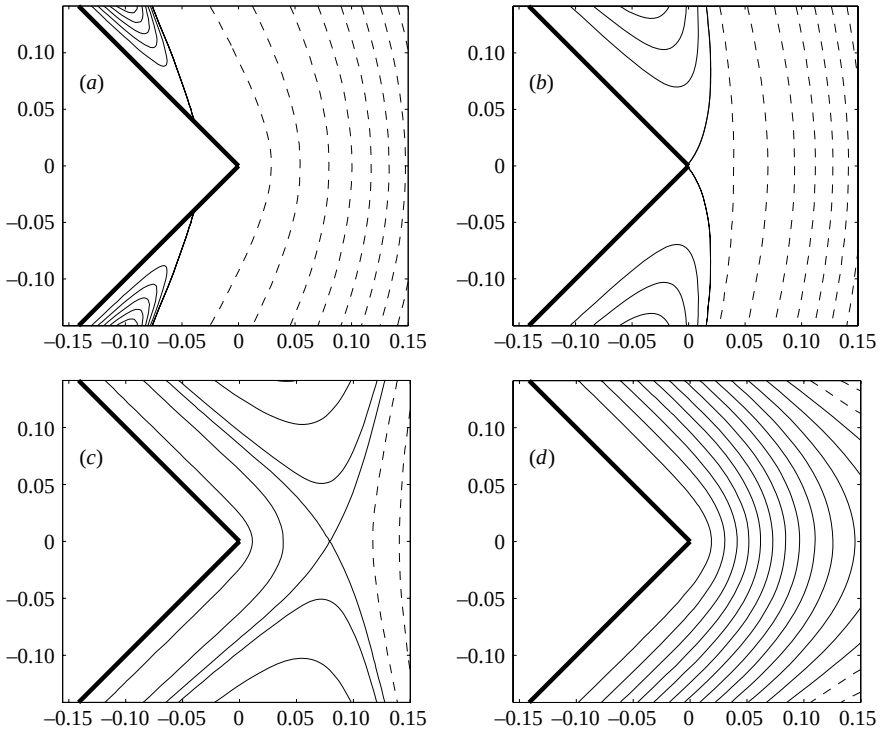

FIGURE 8. Flow evolution near a corner of a reflex angle 270° (regime II of the oscillating-lid problem; regime IV of the oscillating-cylinder problem); this does not involve any eddies during the reversal process. (*a*) $t=\pi/2+0.0016$, (*b*) $t=\pi/2+0.0019$, (*c*) $t=\pi/2+0.0022$, (*d*) $t=\pi/2+0.0025$.

which has a solution in the form

$$\hat{\psi}_0 = \sum_{n=1}^{\infty} A_n f_n(\theta) r^{\lambda_n} + r\left(\frac{\cos\alpha\,(\theta\sin\theta) - \alpha\sin\alpha\cos\theta}{\sin 2\alpha + 2\alpha} + \frac{\sin\alpha\,(\theta\cos\theta) - \alpha\cos\alpha\sin\theta}{\sin 2\alpha - 2\alpha}\right), \tag{4.20}$$

where the infinite sum, as in (4.9), represents the eigensolution of the homogeneous problem and the particular solution (Goodier 1934; Taylor 1962) satisfies the boundary conditions (4.19).

At the first order, the inhomogeneous problem reduces to

$$\nabla^4\hat{\psi}_1(r,\theta) = \chi, \qquad \hat{\psi}_1 = \frac{\partial\hat{\psi}_1}{\partial\theta} = 0, \quad \text{on} \quad \theta = \pm\alpha, \tag{4.21}$$

where

$$\chi = 4\mathrm{i}\sum_{n=1}^{\infty} A_n(1-\lambda_n)\cos\lambda_n\alpha\,\cos(\lambda_n-2)\theta\, r^{\lambda_n-2} + \frac{\mathrm{i}}{r}\frac{4\alpha\cos(\theta-\alpha) - 2\cos(\theta+\alpha)\sin 2\alpha}{4\alpha^2 - \sin^2 2\alpha}. \tag{4.22}$$

The solution of (4.21) can be written as

$$\hat{\psi}_1 = \mathrm{i}\sum_{n=1}^{\infty}(c_n\mathrm{Re}[f_n(\theta)r^{\lambda_n}] + d_n\mathrm{Im}[f_n(\theta)r^{\lambda_n}]) + \mathrm{i}\sum_{n=1}^{\infty}(a_n\mathrm{Re}[h_n(\theta)r^{\lambda_n+2}] + b_n\mathrm{Im}[h_n(\theta)r^{\lambda_n+2}]) + \mathrm{i}r^3 z(\theta), \tag{4.23}$$

where

$$z(\theta) = C_1\cos\theta + C_2\sin\theta + C_3\sin 3\theta + C_4\cos 3\theta - \frac{12(\theta-\alpha)\cos(\theta-\alpha) - 12\theta(\cos(\theta+3\alpha) + 4\alpha\sin(\theta-\alpha)) + 6\sin 2\alpha\cos(\theta+\alpha)}{192(4\alpha^2 - \sin^2 2\alpha)}, \tag{4.24}$$

and the coefficients $C_1, \ldots, C_4$ are given by

$$\left.\begin{aligned} C_1 &= \frac{(8\cos^4\alpha - 12\cos^2\alpha + 3)\alpha^2 + \cos^2\alpha\sin 2\alpha(3 - 4\cos^2\alpha)\alpha + 3\cos^2\alpha\sin^2\alpha\cos 2\alpha}{32\cos^2\alpha\sin\alpha(4\alpha^2 - \sin^2 2\alpha)},\\ C_2 &= \frac{(1 - 4\cos^2\alpha\cos 2\alpha)\alpha^2 + \sin^2\alpha\sin 2\alpha(4\cos^2\alpha - 1)\alpha + 3\cos^2\alpha\sin^2\alpha\cos 2\alpha}{32\cos\alpha\sin^2\alpha(4\alpha^2 - \sin^2 2\alpha)},\\ C_3 &= \frac{1}{128\cos\alpha\sin^2\alpha},\\ C_4 &= \frac{1}{128\cos^2\alpha\sin\alpha}. \end{aligned}\right\} \tag{4.25}$$

As in the remote-corner case, the coefficients a_n, b_n, c_n, d_n in (4.20), (4.23) are all real and the time-dependent streamfunction is again given by (4.17).

Near $r = 0$, $\hat{\psi}_0$ is always dominated by the driven component (since $\mathrm{Re}[\lambda_1] > 1$), so

$$\hat{\psi}_0 \sim r\left(\frac{\cos\alpha(\theta\sin\theta) - \alpha\sin\alpha\cos\theta}{\sin 2\alpha + 2\alpha} + \frac{\sin\alpha(\theta\cos\theta) - \alpha\cos\alpha\sin\theta}{\sin 2\alpha - 2\alpha}\right), \tag{4.26}$$

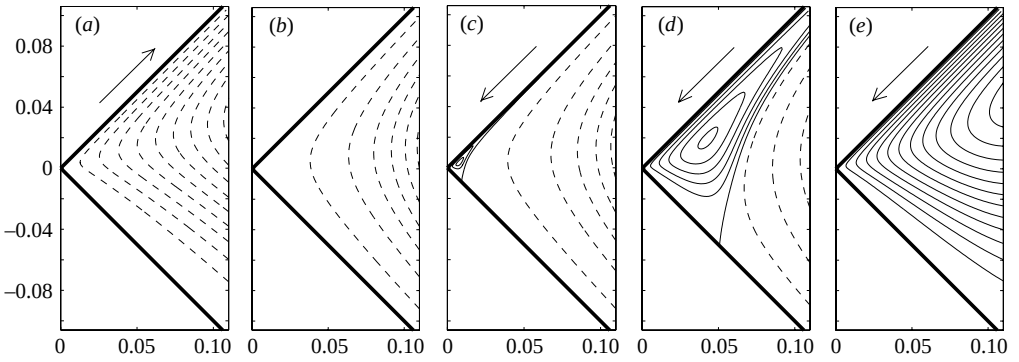

FIGURE 9. Emergence of a single eddy during flow reversal in a corner adjacent to the oscillating lid when $2\alpha \lesssim 126.5^\circ$; in this example $2\alpha = 90^\circ$ and $\eta = 0.1$. (*a*) $t = \pi/2 - 10^{-3}$, (*b*) $t = \pi/2$, (*c*) $t = \pi/2 + 10^{-5}$, (*d*) $t = \pi/2 + 3 \times 10^{-5}$, (*e*) $t = \pi/2 + 3 \times 10^{-3}$.

and the asymptotic behaviour of $\hat{\psi}_1$ is in general

$$\hat{\psi}_1 \sim \mathrm{i}c_1 \mathrm{Re}[f_1(\theta) r^{\lambda_1}] + \mathrm{i}d_1 \mathrm{Im}[f_1(\theta) r^{\lambda_1}] + \mathrm{i}a_1 \mathrm{Re}[h_1(\theta) r^{\lambda_1+2}] + \mathrm{i}b_1 \mathrm{Im}[h_1(\theta) r^{\lambda_1+2}] + \mathrm{i}r^3 z(\theta). \quad (4.27)$$

Provided $\mathrm{Re}[\lambda_1] > 3$, i.e. for $2\alpha \lesssim 126.5^\circ$ (see figure 10*a*), both $\hat{\psi}_0$ and $\hat{\psi}_1$ are dominated by the driven component. Consequently, at most a finite number of eddies appears in the streamline pattern of Ψ (given by (4.17)) during the flow reversal and disappears when the reversal is complete.

A sequence of snapshots of the resulting time-periodic flow in a corner of angle $2\alpha = 90^\circ$ is shown in figure 9 for $\eta = 0.1$. For most of the period, there are no eddies in the corner and the flow structure has the well-known Taylor–Goodier similarity form. As in the remote-corner situation, the flow reversal occurs within a very small time interval (see (4.5)) when the two competing terms in Ψ become comparable in magnitude. When the lid velocity reverses, a single eddy emerges from the corner and rapidly expands along the accelerating lid. This growing eddy rotates in the opposite sense to the base flow and (typically) merges with its counterpart generated in the other corner adjacent to the lid, as shown for example in figure 4(*c*, *d*). The single 'lid eddy' created in this process is later involved in the generation of the heteroclinic streamline (figure 4*e*) and flow reversal in the interior discussed in § 3.

Determination of the local flow structure when $2\alpha \gtrsim 126.5^\circ$ is more subtle and we defer a thorough analysis of this problem to a subsequent paper.

4.1.2. *Oscillating cylinder*

In this case the sequence starts from the first-order solution which, near a corner, has the local form

$$\hat{\psi}_1 = \mathrm{i} \sum_{n=1}^{\infty} (a_n \mathrm{Re}[f_n(\theta) r^{\lambda_n}] + b_n \mathrm{Im}[f_n(\theta) r^{\lambda_n}]) + \mathrm{i}g(\theta) r^4, \quad (4.28)$$

where

$$g(\theta) = \frac{1}{64} \left(\frac{\sin 2\alpha \cos 4\theta - 2 \sin 4\alpha \cos 2\theta}{\sin 2\alpha \cos 4\alpha - 2 \sin 4\alpha \cos 2\alpha} - 1 \right). \quad (4.29)$$

The first term in (4.28) is again a sum of eigensolutions of the biharmonic equation, the (real) coefficients a_n, b_n being determined in principle only when the global geometry of the fluid domain is specified; the second term is the particular solution of the inhomogeneous equation.

At the second order, $\hat{\psi}_2$ satisfies the inhomogeneous equation

$$\nabla^4\hat{\psi}_2 = \chi, \quad \hat{\psi}(r, \pm\alpha) = \frac{\partial\hat{\psi}}{\partial\theta}\bigg|_{\theta=\pm\alpha} = 0, \tag{4.30}$$

where

$$\chi(r,\theta) = \mathrm{i}\nabla^2\psi_1 = 4\mathrm{i}\sum_{n=1}^{\infty} A_n(1-\lambda_n)\cos\lambda_n\alpha\,\cos(\lambda_n-2)\theta\, r^{\lambda_n-2} - \frac{(3\cos 2\theta - 4\cos 2\alpha)\sin 4\alpha + 2\sin 2\alpha\cos 4\alpha}{8\sin 2\alpha(1+2\cos^2 2\alpha)}\, r^2. \tag{4.31}$$

Consequently, the second-order solution $\hat{\psi}_2$ can be written as

$$\hat{\psi}_2 = \sum_{n=1}^{\infty}(c_n\mathrm{Re}[f_n(\theta)r^{\lambda_n}] + d_n\mathrm{Im}[f_n(\theta)r^{\lambda_n}]) - \sum_{n=1}^{\infty}(a_n\mathrm{Re}[h_n(\theta)r^{\lambda_n+2}] + b_n\mathrm{Im}[h_n(\theta)r^{\lambda_n+2}]) + w(\theta)r^6, \tag{4.32}$$

where $f_n(\theta)$ and $h_n(\theta)$ are given by (4.10) and (4.16), and

$$4608\, w(\theta) = -\frac{\cos 2\alpha\cos 6\theta}{8\cos^4 2\alpha - 3\cos 4\alpha} - \frac{6(\cos 4\alpha - 4\cos^4 2\alpha)\cos 4\theta}{(2\cos^2 2\alpha+1)(8\cos^4 2\alpha - 3\cos 4\alpha)} - \frac{(9\cos 2\theta - 8\cos 2\alpha)\cos 2\alpha + 2\cos 4\alpha}{2\cos^2 2\alpha + 1} \tag{4.33}$$

is the particular solution associated with the inhomogeneous term $-\nabla^2(g(\theta)r^4)$.

As previously noted, $\hat{\psi}_1$ is purely imaginary and $\hat{\psi}_2$ is real (and so therefore are their asymptotic expansions near the corner). The real time-dependent streamfunction $\Psi(x, y, t)$ is therefore given by

$$\Psi(x,y,t) = \mathrm{Re}[\hat{\psi}\mathrm{e}^{\mathrm{i}t}] = -\eta\hat{\psi}_1\sin t + \eta^2\hat{\psi}_2\cos t + O(\eta^3). \tag{4.34}$$

We note again here that if only the leading-order term is retained in (4.34), then the evolution is quasi-steady, and it is the higher-order correction that reveals the evolution of flow topology associated with the flow-reversal process. The time scale of this process is again of order η.

Near $r = 0$, the dominant terms of (4.28) and (4.32) are

$$\left.\begin{aligned} &\hat{\psi}_1 \sim \mathrm{i}a_1\mathrm{Re}[f_1(\theta)r^{\lambda_1}] + \mathrm{i}b_1\mathrm{Im}[f_1(\theta)r^{\lambda_1}] + \mathrm{i}g(\theta)r^4 \qquad \text{as} \quad r\to 0,\\ &\hat{\psi}_2 \sim c_1\mathrm{Re}[f_1(\theta)r^{\lambda_1}] + d_1\mathrm{Im}[f_1(\theta)r^{\lambda_1}]\\ &\quad -a_1\mathrm{Re}[h_1(\theta)r^{\lambda_1+2}] - b_1\mathrm{Im}[h_1(\theta)r^{\lambda_1+2}] + w(\theta)r^6 \qquad \text{as} \quad r\to 0. \end{aligned}\right\} \tag{4.35}$$

As for the lid-corner case, there is here a competition between the driven components and the eigen-components in the two solutions. If the eigen-component dominates sufficiently near the corner and if $\mathrm{Im}[\lambda_1] \neq 0$, then there will be an infinite sequence of eddies in the structure. If, on the other hand, the driven component

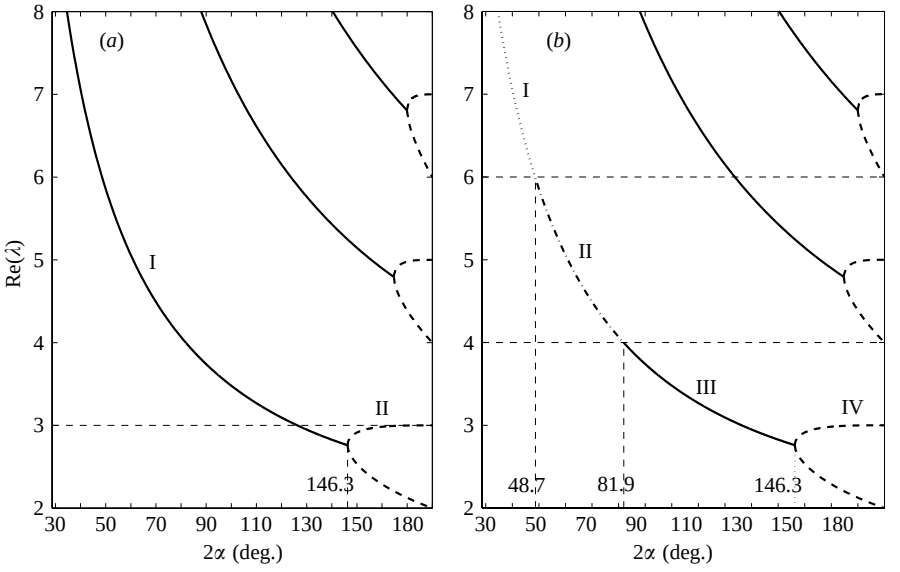

FIGURE 10. Real parts of $\lambda_1, \lambda_2, \lambda_3, \ldots$ (see (4.12)) and different dynamical regimes of local flow near a sharp corner as a function of the corner angle 2α. (*a*) Oscillating-lid case (flow given by (4.17)): regime I – there is infinite sequence of time-dependent corner eddies in the flow throughout the time-periodic evolution; regime II – there is (at most) one eddy generated during flow reversal. (*b*) Oscillating-cylinder case (flow given by (4.34)): regimes III (solid) and IV (dashed) characterized as, respectively, I and II in (*a*) above; regime II (dash-dotted) – an infinite sequence of eddies is present at some stage of the reversal process (it must disappear at least for $t = \frac{1}{2}\pi(2k+1)$); regime I (dotted) – at most a finite number of time-dependent eddies appear at some stage of the reversal process.

dominates near the corner, there can be at most a finite sequence of eddies in any neighbourhood of the corner. From (4.35), it is evident that $\hat{\psi}_1$ contains such an infinite sequence provided $\mathrm{Re}[\lambda_1] < 4$, $\mathrm{Im}[\lambda_1] \neq 0$, i.e. provided $81.9^\circ \lesssim 2\alpha \lesssim 146.2^\circ$, and similarly that $\hat{\psi}_2$ contains such a sequence provided $\mathrm{Re}[\lambda_1] < 6$, $\mathrm{Im}[\lambda_1] \neq 0$, which corresponds to $48.7^\circ \lesssim 2\alpha \lesssim 146.2^\circ$. Combining this information about ψ_1 and ψ_2 to determine the flow structure given by Ψ, we obtain four distinct regimes of corner angles characterized by different topological evolution (see figure 10*b*):

Regime I ($2\alpha \lesssim 48.7^\circ$): there may be at most a finite number of eddies in the corner. Both $\hat{\psi}_1$ and $\hat{\psi}_2$ are dominated by the driven component.

Regime II ($48.7^\circ \lesssim 2\alpha \lesssim 81.9^\circ$): an infinite structure of time-dependent eddies appears during the flow reversal and disappears when the reversal is complete. In this regime, $\hat{\psi}_2$ is dominated by the eigen-component and contains the infinite structure of eddies but $\hat{\psi}_1$ is dominated by the driven component.

Regime III ($81.9^\circ \lesssim 2\alpha \lesssim 146.2^\circ$): an infinite structure of time-dependent eddies is present throughout the whole time-periodic evolution. Both $\hat{\psi}_1$ and $\hat{\psi}_2$ are dominated by the eigen-component (just as for the oscillating-lid situation).

Regime IV ($2\alpha \gtrsim 146.2^\circ$): at most one single eddy appears during the flow reversal. In this regime, λ_1 is real, so neither $\hat{\psi}_1$ nor $\hat{\psi}_2$ contains an infinite eddy sequence.

The local flow structure in regimes III and IV, when the corner flow is dominated by the eigen-component, is basically the same as in the oscillating-lid case (figures 6–8).

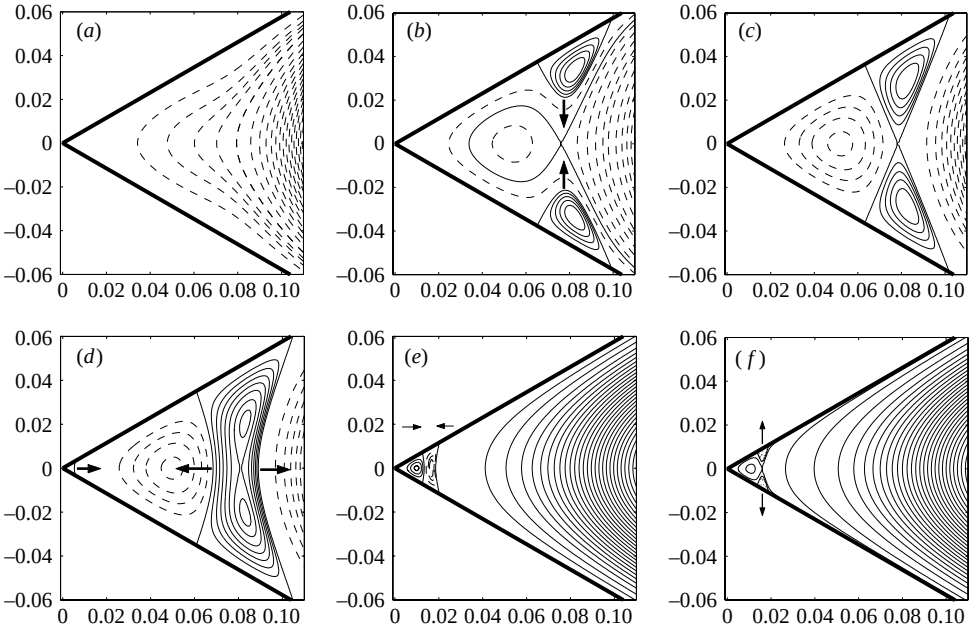

FIGURE 11. Initial stage of flow reversal in an oscillating cylinder near a sharp corner representative of regime II (see text); $2\alpha = 60^\circ$, $\eta = 0.1$ in this example. The sequence of snapshots of instantaneous streamline patterns of Ψ (4.34) illustrates crucial stages of the time-periodic evolution in the non-inertial frame oscillating with the cylinder: (*a*) $t = \pi - 0.00018$, (*b*) $t = \pi - 0.00015$, (*c*) $t = \pi - 0.0001457$, (*d*) $t = \pi - 0.00014$, (*e*) $t = \pi - 0.000024$, (*f*) $t = \pi - 0.000026$. Such pairs of sidewall eddies are also involved in the flow reversal in corner angles from regime I but, in contrast to the situation in regime II, they are only finite in number.

Note that the structure of the local flow in the square, presented in figure 1, belongs to regime III.

In order to illustrate the flow evolution in regimes I and II, we close the domain with a circular arc at $r = 1$ and impose the no-slip conditions on the boundary. As in the oscillating-lid problem, we again use the least-squares technique to determine the first 20 coefficients a_n, b_n, c_n, d_n. A sequence of snapshots of instantaneous streamline patterns of Ψ given by (4.34) is shown in figure 11 (see also figure 5*c*, *d*) for $2\alpha = 60^\circ$ and $\eta = 0.1$ ($a_1 \approx 228 \times 10^{-5}$, $b_1 \approx -1.4 \times 10^{-5}$, $c_1 \approx 7.7 \times 10^{-5}$, $d_1 \approx -0.01 \times 10^{-5}$). Based on the above analysis, we know that in this case an infinite sequence of counter-rotating eddies must appear in the flow during the reversal process. This is achieved by the emergence of sidewall eddies that rotate in the opposite sense to the main body of the fluid. These eddies later merge into one oppositely rotating eddy (figure 11*c*) and the two dividing streamlines created in such a process begin to travel in opposite directions (figure 11*d*). At this stage the infinite structure of time-dependent corner eddies exists in the flow. This structure is then destroyed by the reverse process. As shown by figure 11(*d*), pairs of dividing streamlines created in similar events nearer the corner approach each other and later divide the eddy into pairs of sidewall eddies which are annihilated at the walls. Note here that the local flow near the 60° corner in figure 3 belongs to regime II, although only one pair of emerging sidewall eddies is visible in the global picture.

The sidewall eddies are also responsible for initiation of the flow reversal in corners in regime I but in this case only a finite number of such pairs is created as opposed

to the infinite sequence being generated in the regime II case. Note here that the example of flow reversal shown in figure 2, where such sidewall eddies appear in the acute-angle corners ($2\alpha = \pi/4$), represents evolution that is characteristic of regime I and therefore involves a finite number of eddies. In the obtuse angles of the rhombus ($2\alpha = 135^\circ$) (regime III) an infinite sequence of eddies must be present throughout the cycle, but these are too small to be observed on the scale of figure 2.

5. The high-η limit for the oscillating-cylinder problem

Computations indicate that the qualitative character of the flow reversal changes when η is increased beyond about 200. Here we simply analyse the asymptotic behaviour for the oscillating-cylinder problem when the oscillation frequency is large, $\eta \gg 1$. (The oscillating-lid problem may be similarly treated.) We anticipate that a boundary layer of thickness $O(\eta^{-1/2})$ will form on the inner side of $\partial\mathscr{D}$. Let (s, n) be tangential and normal coordinates on $\partial\mathscr{D}$, with n pointing inwards. The boundary layer then occupies the region $n \sim O(\eta^{-1/2})$, and we may refer to the interior region $n \gg \eta^{-1/2}$ as the 'core'. In the core, viscous effects are negligible, and at leading order (from (2.9)) the core streamfunction $\hat{\psi}_0(x, y)$ satisfies

$$\nabla^2 \hat{\psi}_0 = 1. \tag{5.1}$$

This represents an inviscid flow of uniform vorticity -1, on which we can impose only the single boundary condition

$$\hat{\psi}_0 = 0 \quad \text{on} \quad \partial\mathscr{D}. \tag{5.2}$$

The solution $\hat{\psi}_0(x, y)$ of (5.1), (5.2) is uniquely determined and real. Relative to the inertial (laboratory) frame of reference, this flow is irrotational. It is of historic interest to note that the problem (5.1), (5.2) was in fact solved for a rectangular domain in terms of Fourier series by Stokes (1843), two years before his famous derivation of the Navier–Stokes equations.

Of course, $\hat{\psi}_0(x, y)$ does not satisfy the no-slip condition $\partial\hat{\psi}/\partial n = 0$ on $\partial\mathscr{D}$, and this is why a boundary layer is needed. The 'slip' velocity at the inner edge of this boundary layer is

$$\hat{V}(s) = \left.\frac{\partial\hat{\psi}_0}{\partial n}\right|_{\partial D} = \eta^{1/2}\left.\frac{\partial\hat{\psi}_0}{\partial\tilde{n}}\right|_{\partial D}, \tag{5.3}$$

where $\tilde{n} = \eta^{1/2} n$. In the layer, $\nabla^2 = \eta^{-1}\partial^2/\partial\tilde{n}^2$, and the tangential velocity component $\hat{v}(s, \tilde{n})(= \partial\hat{\psi}/\partial\tilde{n})$ satisfies

$$\mathrm{i}\hat{v} = \mathrm{i}\hat{V}(s) + \frac{\partial^2\hat{v}}{\partial\tilde{n}^2} \tag{5.4}$$

where the term $\mathrm{i}\hat{V}(s)$ represents the tangential pressure gradient imposed on the boundary layer by the core flow. The relevant boundary conditions are

$$\left.\begin{aligned} \hat{v}(s, \tilde{n}) &= 0 \qquad \text{on} \quad \tilde{n} = 0, \\ \hat{v}(s, \tilde{n}) &\sim \hat{V}(s) \quad \text{as} \quad \tilde{n} \to \infty, \end{aligned}\right\} \tag{5.5}$$

and the solution (an oscillating Stokes layer) is

$$\hat{v}(s, \tilde{n}) = \hat{V}(s)\left(1 - \mathrm{e}^{-(1+\mathrm{i})\tilde{n}/2}\right). \tag{5.6}$$

The flux in this layer relative to the core slip velocity is

$$\hat{Q} = -\int_0^\infty \hat{V}(s)\mathrm{e}^{-(1+\mathrm{i})\tilde{n}/2}\,\mathrm{d}n = -(1 - \mathrm{i})\hat{V}(s). \tag{5.7}$$

Incompressibility then requires that there is a normal component of velocity $\hat{U}$ from the boundary layer to the core given by

$$\hat{U} = -\frac{\mathrm{d}\hat{Q}}{\mathrm{d}s} = (1-\mathrm{i})\frac{\mathrm{d}\hat{V}}{\mathrm{d}s} \tag{5.8}$$

(an effect akin to Ekman suction). This drives a correction $\eta^{-1/2}\hat{\psi}_1(x, y)$ to the core flow given by

$$\nabla^2\hat{\psi}_1 = 0 \tag{5.9}$$

with the boundary condition

$$\frac{\partial\hat{\psi}_1}{\partial s} = -\hat{U}(s) = -(1-\mathrm{i})\frac{\mathrm{d}\hat{V}}{\mathrm{d}s} \quad \text{on} \quad \partial\mathscr{D}, \tag{5.10}$$

or equivalently

$$\hat{\psi}_1 = -(1-\mathrm{i})\hat{V}(s) \quad \text{on} \quad \partial\mathscr{D}. \tag{5.11}$$

The solution to (5.9), (5.11) is uniquely determined, and we now have the solution to (2.9) in the form

$$\hat{\psi}(x, y) = \hat{\psi}_0(x, y) + \eta^{-1/2}\hat{\psi}_1(x, y) + O(\eta^{-1}), \tag{5.12}$$

where the $O(\eta^{-1})$ term could in principle be found by an iterative technique. Since $\hat{V}(s)$ is real, it is evident that

$$\hat{\psi}_1 = (1-\mathrm{i})\hat{\psi}_{1r}(x, y) \tag{5.13}$$

where $\hat{\psi}_{1r}$ is real, and from (2.10) we then have Ψ in the form

$$\Psi = \left(\hat{\psi}_0 + \eta^{-1/2}\hat{\psi}_{1r}\right)\cos t + \eta^{-1/2}\hat{\psi}_{1r}\sin t + O(\eta^{-1}). \tag{5.14}$$

Just as for the low-η situation, the correction here is out of phase with the leading-order solution. This yields a smooth change of topology associated with the reversal of the core flow.

The leading-order solution $\hat{\psi}_0\cos t$ vanishes when $t_n = (n+\frac{1}{2})\pi$ ($n = 0, \pm1, \pm2, \ldots$). For most of the cycle, the streamline topology is just that of $\hat{\psi}_0(x, y)$. However, in each small time interval

$$\Delta t_n = \left(t_n - \tfrac{1}{2}\Delta t, t_n + \tfrac{1}{2}\Delta t\right), \quad \Delta t = O\left(\eta^{-1/2}\right), \tag{5.15}$$

the out-of-phase correction $\eta^{-1/2}\hat{\psi}_{1r}\sin t$ is comparable in magnitude with $\hat{\psi}_0\cos t$. During each such time interval

$$\Psi(x, y, t) \approx (-1)^n\eta^{-1/2}[\hat{\psi}_{1r}(x, y) - \tau\hat{\psi}_0(x, y)] \tag{5.16}$$

where $\tau = \eta^{1/2}t$. As for the low-η situation, this approximation is sufficient to describe the flow reversal as the scaled time increases through zero from large negative to large positive values.

5.1. *Flow near a corner*

Here, the solution of (5.1), (5.2) consists of the particular integral

$$\hat{\psi}_{0P} = \tfrac{1}{4}r^2\left(1 - \frac{\cos 2\theta}{\cos 2\alpha}\right), \tag{5.17}$$

and the complementary function

$$\hat{\psi}_{0C} = Ar^{\pi/2\alpha} \cos \frac{\pi\theta}{2\alpha}. \tag{5.18}$$

The term on the right-hand side of (5.17) dominates near $r = 0$ if $2\alpha < \pi/2$, while the term on the right-hand side of (5.18) dominates if $2\alpha > \pi/2$ (the implications of this distinction have been noted in a different context by Moffatt & Duffy 1980). Let us consider these cases separately.

(i) *Flow near an acute-angle corner* ($2\alpha < \pi/2$). Here $\hat{\psi} \sim \hat{\psi}_{0P}$ near $r = 0$, so

$$\hat{V}(r) = \frac{1}{r}\frac{\partial \hat{\psi}_{0P}}{\partial \theta} = -\tfrac{1}{2} r \tan 2\alpha \quad \text{on} \quad \theta = \pm\alpha. \tag{5.19}$$

Hence, the boundary conditions for $\hat{\psi}_1$ are

$$\hat{\psi}_1 = \tfrac{1}{2}(1 - \mathrm{i}) r \tan 2\alpha \quad \text{on} \quad \theta = \pm\alpha. \tag{5.20}$$

The relevant solution of $\nabla^2 \hat{\psi}_1 = 0$ is therefore

$$\hat{\psi}_1 = \tfrac{1}{2}(1 - \mathrm{i}) \frac{\tan 2\alpha}{\cos \alpha} r \cos \theta = (1 - \mathrm{i}) \frac{\sin \alpha}{\cos 2\alpha} r \cos \theta. \tag{5.21}$$

The composite solution for $\hat{\psi}$ is thus

$$\hat{\psi} = \tfrac{1}{4} r^2 \left(1 - \frac{\cos 2\theta}{\cos 2\alpha}\right) + \eta^{-1/2}(1 - \mathrm{i}) \frac{\sin \alpha}{\cos 2\alpha} r \cos \theta + O(\eta^{-1}). \tag{5.22}$$

This description is valid only if $\eta^{-1/2} r \ll r^2$, i.e. $r \gg \eta^{-1/2}$, so that the first term is indeed dominant; the description holds in the range of intermediate asymptotics (Barenblatt 1996)

$$\eta^{-1/2} \ll r \ll 1, \tag{5.23}$$

the second part of this inequality meaning simply that we are in a corner region on a scale small compared with that of the whole domain $\mathscr{D}$. The first part of the inequality is to be expected, because the boundary layers on $\theta = \pm\alpha$ overlap in the region $r = O(\eta^{-1/2})$ and the simple boundary-layer description is no longer valid; indeed, for $r \ll \eta^{-1/2}$, we revert to the viscosity-dominated regime where the oscillations characteristic of the Stokes-layer velocity profiles give way to the radial oscillations associated with corner eddies.

From (5.16), we find that at an intermediate distance from the corner the flow reversal during the time interval Δt_n is approximately given by

$$\Psi(x, y, \tau) \approx (-1)^n \eta^{-1/2} \left[\frac{\sin \alpha}{\cos 2\alpha} r \cos \theta - \tau \frac{r^2}{4}\left(1 - \frac{\cos 2\theta}{\cos 2\alpha}\right)\right]. \tag{5.24}$$

This reversal process in the core region is described by the sequence shown in figure 12. For $\tau < 0$, a saddle point located at $r \sim O(-1/\tau)$, $\theta = 0$ propagates from the origin towards large r; for $\tau > 0$, the streamline shape gradually recovers to that of the zero-order solution. Of course the intersection of the streamlines with the boundary is only apparent; in reality they adjust to become parallel to the boundary (and to satisfy the no-slip condition) within the boundary layer. The saddle point which propagates from the origin in this approximation is in fact created in the boundary layer when the emerging corner eddy is consumed by the two expanding 'wall eddies' (compare with figure 14*c*, *d*)

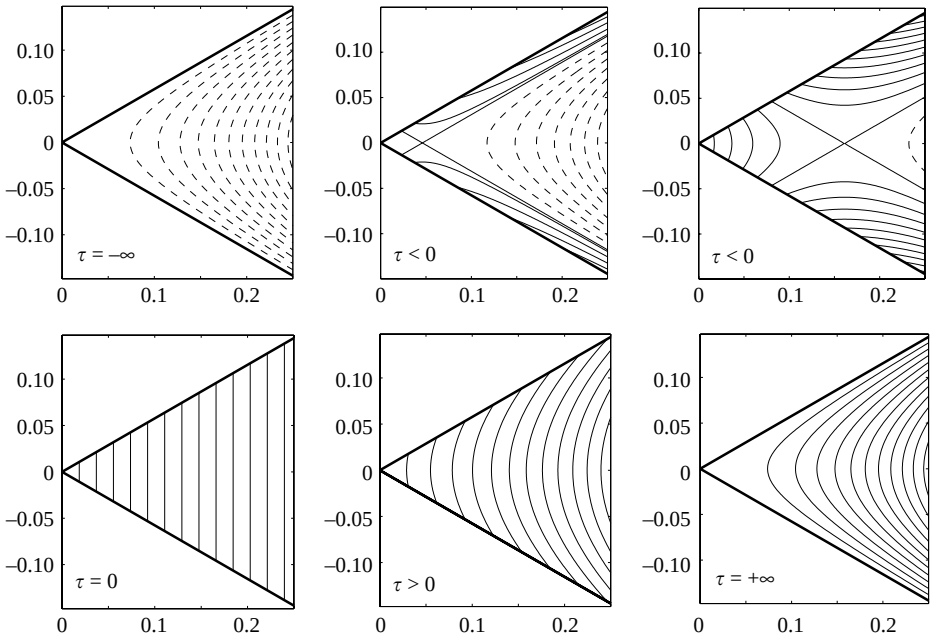

FIGURE 12. Sketch of flow reversal in a corner for $2\alpha < \pi/2$ in the high-η limit based on the (approximate) solution (5.24); $2\alpha = 60^\circ$ in this example. This description is valid only for $\eta^{-1/2} \ll r \ll 1$ and outside boundary layers on $\theta = \pm\alpha$.

(ii) *Flow near an obtuse-angle corner* ($2\alpha > \pi/2$). In this case, near $r = 0$, we obtain

$$\hat{\psi} \sim \hat{\psi}_{0C} = Ar^{\pi/2\alpha} \cos\frac{\pi\theta}{2\alpha}, \tag{5.25}$$

where A is a constant (which we may suppose real by choice of time origin) determined in principle by the global geometry of the domain $\mathscr{D}$. It follows by the same procedure as before that the composite solution for $\hat{\psi}$ is

$$\hat{\psi} = Ar^{\pi/2\alpha}\left(\cos\frac{\pi\theta}{2\alpha} - \eta^{-1/2}(1-\mathrm{i})\frac{\pi}{2\alpha r}\frac{\cos(\pi/2\alpha-1)\theta}{\cos(\pi/2\alpha-1)\alpha}\right) + O(\eta^{-1}), \tag{5.26}$$

and, at the intermediate distance from the corner, the flow reversal during Δt_n is described by

$$\Psi(x, y, \tau) \approx (-1)^{n+1}\eta^{-1/2}Ar^{\pi/2\alpha}\left[\frac{\pi}{2\alpha r}\frac{\cos(\pi/2\alpha-1)\theta}{\cos(\pi/2\alpha-1)\alpha} + \tau\cos\frac{\pi\theta}{2\alpha}\right]. \tag{5.27}$$

Here, the first term actually gives a singular velocity at $r = 0$; but again the description is valid only for $r \gg \eta^{-1/2}$. Nevertheless the reversal, originating as it does from the neighbourhood of the origin due to the viscous process discussed in § 4, has a more explosive character in this case. The corresponding reversal process in the core region is described by the sequence shown in figure 13.

5.2. *Flow reversal in a square domain, $\eta \gg 1$*

Consider now an example of a flow reversal inside a square domain at large η. An appropriate global solution of (2.9), (2.10) (with $\Lambda = 1$) can be determined using either the analytical method (A 1)–(A 6) described in Appendix, or by means of a finite-difference algorithm.

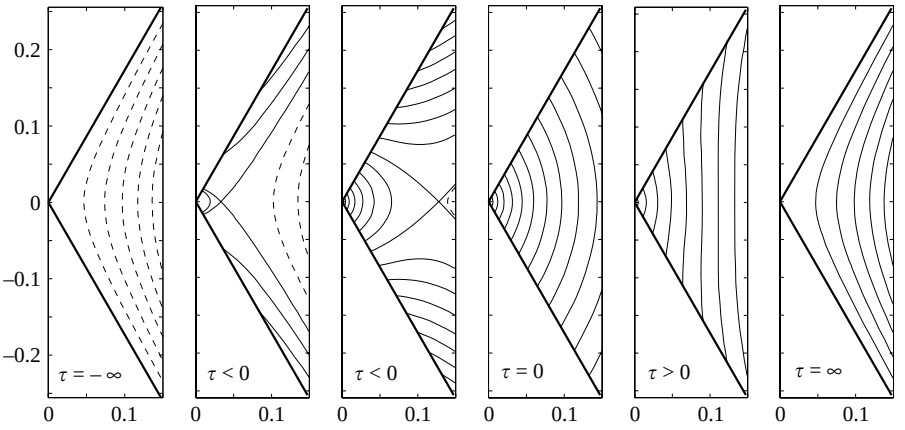

FIGURE 13. Sketch of flow reversal in the core region of a corner for $2\alpha > \pi/2$ in the high-η limit based on the (approximate) solution (5.27); $2\alpha = 120^\circ$ in this example. This description is valid only for $\eta^{-1/2} \ll r \ll 1$ and outside boundary layers on $\theta = \pm\alpha$.

Figure 14 presents the time-periodic evolution of the flow as a sequence of snapshots of instantaneous streamline patterns of the streamfunction $\Psi(x, y, t)$, given by (2.10), for $\eta = 2000$. As for the low-η regime (figure 1), four eddies emerge from the corners at the onset of the flow reversal. These counter-rotate relative to the central eddy (dashed lines). As discussed in the previous sections, even in the high-η situation the flow structure very near the corner ($r \sim O(\eta^{-1/2})$) is described by (4.28), (4.32) and (4.34) with $2\alpha = \pi/2$ (regime III). At the intermediate distance from the corner ($\eta^{-1/2} \ll r \ll 1$), the behaviour involves both $\hat{\psi}_{0C}$ and $\hat{\psi}_{0P}$, given by (5.18) and (5.17), which have the same order of magnitude. As shown by Moffatt & Duffy (1980), in the particular situation of the right-angle corner, a compromise is achieved for which the streamfunction is $O(r^2 \ln r)$ as $r \to 0$. However, in contrast to the low-η situation, the primary corner eddies do not expand into the interior in this case but merge together with the four 'wall eddies' (figure 14*b*, *c*, *d*) in the Stokes boundary layers which dominate the flow structure near the boundary (figure 14*d–h*). The centres of these eddies move very little during the subsequent stage of flow reversal. Eventually, the central eddy is consumed (figure 14*f*) and the fluid in the interior subsequently rotates in the same sense as the boundary (figure 14*g*, *h*, *i*).

Note that this mechanism is different from that identified in the low-η regime where the emerging corner eddies played a primary role in the flow-reversal process in the interior. In the more complex high-η evolution, the corner eddies serve to generate the wall eddies which are then involved in the sequence of global bifurcations of a single heteroclinic orbit that leads to the flow reversal.

In less symmetric domains, which we have also investigated, the reversal mechanism becomes much more complicated, since highly symmetric bifurcations like those revealed in figure 14 are no longer possible. Instead, a number of distinct heteroclinic (and/or homoclinic) connections are created when the dividing streamlines of emerging corner eddies detach from the boundary. These structures are later involved in a series of global bifurcations, leading eventually to the disappearance of the central eddy and reversal of the flow. We conjecture that, regardless of the actual geometry, the generation of the Stokes boundary layer and the dominant role of the wall eddies are common features of the flow-reversal process at large η.

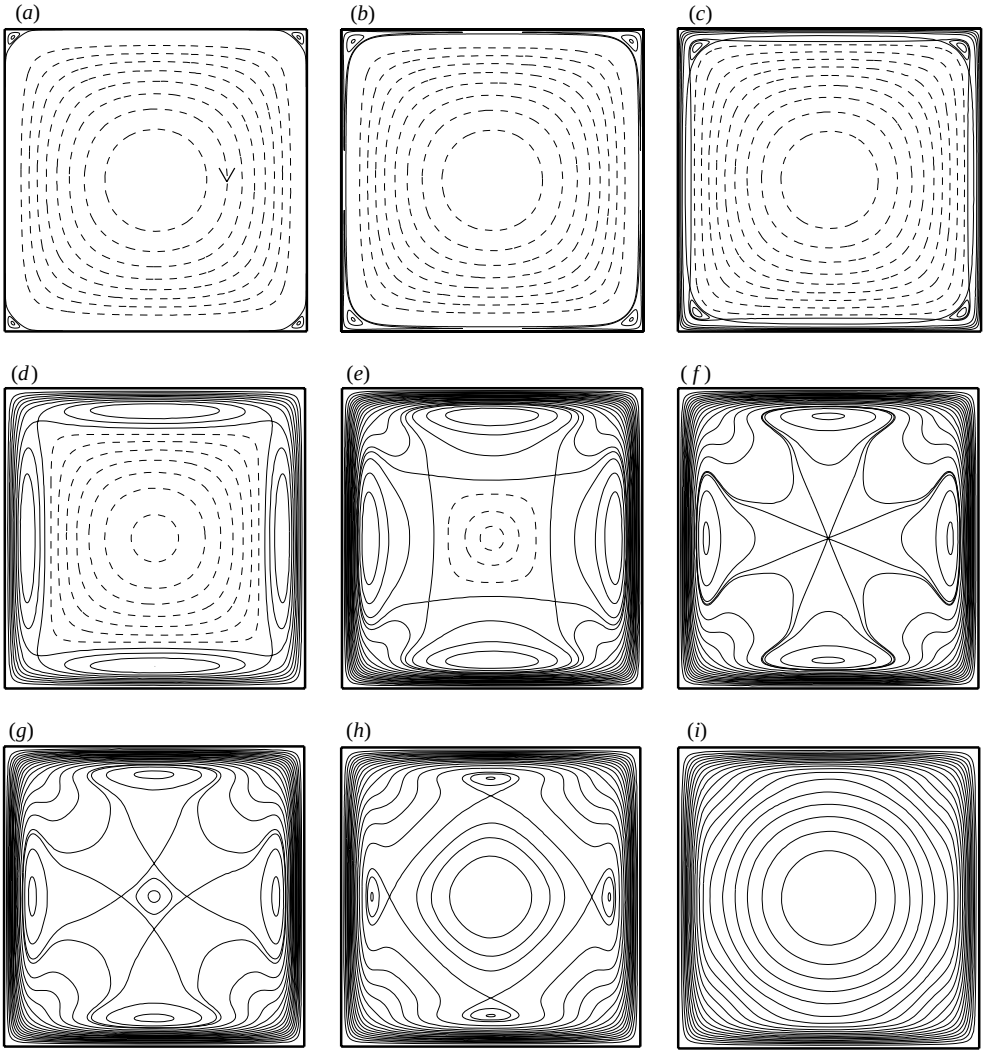

FIGURE 14. Flow reversal inside an oscillating square domain at large η (non-inertial frame oscillating with the cylinder used): sequence of snapshots showing instantaneous streamline patterns at different stages of time-periodic evolution with $\eta = 2000$: (*a*) $t = 0.65$, (*b*) $t = 0.9$, (*c*) $t = 1.2$, (*d*) $t = 1.5$, (*e*) $t = 1.56$, (*f*) $t = \pi/2$, (*g*) $t = 1.572$, (*h*) $t = 1.59$, (*i*) $t = 1.65$. Note that in contrast to the flow reversal at smaller η (figure 1) the corner eddies blend into Stokes layers and associated wall eddies which develop near the boundary; the flow reversal in the interior is realized through a series of global bifurcations involving these wall eddies rather than the primary corner eddies.

6. Conclusions

We have analysed the time-periodic evolution of Stokes flows in a bounded domain, forced either by tangential oscillation of part of the boundary, or by torsional oscillation of the whole domain. The time lag between the motion of the boundary and the response of the contained fluid is captured by retaining the local acceleration term in the governing dynamical equation. This permits a description of the manner in which the internal flow reverses during each half-period of the cycle.

We have focused attention on the behaviour near any sharp corner that may be present on the domain boundary. Depending on the angle of the corner, and on the nature of the forcing, an infinite sequence of corner eddies may be present either during the whole cycle, or just during the reversal process. Eddies originating in the corner region eventually participate in the global flow-reversal process. We have described the topological transitions that occur in the streamline pattern for a variety of domains, and have sought to explain the origin of these transitions through local corner analysis.

We have presented an asymptotic analysis for both small and large values of the dimensionless frequency parameter η. In both situations, the changes of flow topology associated with flow reversal occur during a small time interval centred on the phase of the periodic cycle when the leading-order term vanishes. At low η, this leading-order term is the 'quasi-static' solution of the biharmonic equation with appropriate boundary conditions. At large η, it is (in the oscillating-domain case) the quasi-static potential flow driven by the normal component of velocity at the boundary; in this case, an oscillatory Stokes boundary layer is needed to accommodate the no-slip condition, and there is an interesting interaction between the corner eddies and this boundary layer as the reversal process develops.

This study opens up an interesting range of problems that deserve further study. First, if corners are rounded off, so that the boundary is everywhere analytic, it is to be expected that a finite sequence of eddies may still form in regions near points of maximum curvature on the boundary. It would be interesting to develop a numerical technique for the solution of the oscillating-cylinder problem for an arbitrary smooth boundary. The changing character of the flow as η increases from small to large values would be of special interest, and particularly the question of whether, and in what circumstances, separation of the Stokes boundary layer may occur at large η. Transient behaviour due to the sudden application of boundary forcing also merits study. The analysis could be extended in a straightforward way to fully three-dimensional domains, for which a rich tapestry of topological transitions in time-periodic flow may be anticipated. It should be possible to include nonlinear inertia, and to investigate numerically the effect of increasing Reynolds number for this class of internal flows. Finally, mixing properties of the time-periodic flows discussed in this paper can be studied; a paper on this aspect is in preparation.

M.B. is supported by a scholarship from the Gates Cambridge Trust. H. K. M. acknowledges the support of a Leverhulme Emeritus Professorship.

Appendix. Outline of analytical procedure used for rectangular domain

The elliptic problem (2.9) for the amplitude function $\hat{\psi}$ can be solved by the superposition method (see Mathieu 1881 or Timoshenko & Goodier 1970). This method has been used by Meleshko (1996) for analysis of Stokes flow in a rectangular cavity driven by steady motion of a lid.

Here, we use the method to find $\hat{\psi}$ for the oscillating-cylinder problem given by (2.9) with $\Lambda = 1$ when the cross-section is a rectangle with sides $|x| = 1$ and $|y| = h$. First let

$$\hat{\psi} = \tfrac{1}{2}h\,\mathscr{X} + \left(1 - \tfrac{1}{2}h\right)\mathscr{Y} + \xi(x, y) \tag{A 1}$$

where

$$\left.\begin{aligned}\mathscr{X} &= \frac{\cosh\tfrac{1}{2}\sqrt{\mathrm{i}\eta}-\cosh\sqrt{\mathrm{i}\eta}\,x}{2\sqrt{\mathrm{i}\eta}\sinh\tfrac{1}{2}\sqrt{\mathrm{i}\eta}}+\tfrac{1}{2}\big(x^2-\tfrac{1}{4}\big),\\ \mathscr{Y} &= h\frac{\cosh\tfrac{1}{2}h\sqrt{\mathrm{i}\eta}-\cosh\sqrt{\mathrm{i}\eta}\,y}{2\sqrt{\mathrm{i}\eta}\sinh\tfrac{h}{2}\sqrt{\mathrm{i}\eta}}+\tfrac{1}{2}\big(y^2-\tfrac{1}{4}h^2\big)\end{aligned}\right\} \tag{A 2}$$

are even in x and y respectively. Then ξ satisfies the equation

$$\nabla^2\xi-(\mathrm{i}\eta)^{-1}\nabla^4\xi=0, \tag{A 3}$$

and the boundary conditions

$$\xi\big(x,\,y=\pm\tfrac{1}{2}h\big)=-\tfrac{1}{2}h\mathscr{X},\qquad \left.\frac{\partial\xi}{\partial y}\right|_{y=\pm h/2}=0, \tag{A 4}$$

$$\xi\big(x=\pm\tfrac{1}{2},\,y\big)=-\big(1-\tfrac{1}{2}h\big)\mathscr{Y},\qquad \left.\frac{\partial\xi}{\partial x}\right|_{x=\pm 1/2}=0. \tag{A 5}$$

We now expand ξ as the sum of two Fourier series

$$\xi=\xi_0+h\sum_{m=1}^{\infty}(-1)^m\frac{X_m}{\alpha_m^2}\,p_m(y)\cos\alpha_m x+\sum_{l=1}^{\infty}(-1)^l\frac{Y_l}{\beta_l^2}\,q_l(x)\cos\beta_l y \tag{A 6}$$

where $\alpha_m=2\pi m$, $\beta_l=2\pi l/h$, and

$$p_m(y)=\frac{\sqrt{\alpha_m^2+\mathrm{i}\eta}\sinh\tfrac{1}{2}h\sqrt{\alpha_m^2+\mathrm{i}\eta}\cosh\alpha_m y-\alpha_m\sinh\tfrac{1}{2}h\alpha_m\cosh\sqrt{\alpha_m^2+\mathrm{i}\eta}\,y}{\sqrt{\alpha_m^2+\mathrm{i}\eta}\sinh\tfrac{1}{2}h\sqrt{\alpha_m^2+\mathrm{i}\eta}\cosh\tfrac{1}{2}h\alpha_m-\alpha_m\sinh\tfrac{1}{2}h\alpha_m\cosh\tfrac{1}{2}h\sqrt{\alpha_m^2+\mathrm{i}\eta}} \tag{A 7}$$

$$q_l(x)=\frac{\sqrt{\beta_l^2+\mathrm{i}\eta}\sinh\tfrac{1}{2}\sqrt{\beta_l^2+\mathrm{i}\eta}\cosh\beta_l x-\beta_l\sinh\tfrac{1}{2}\beta_l\cosh\sqrt{\beta_l^2+\mathrm{i}\eta}\,x}{\sqrt{\beta_l^2+\mathrm{i}\eta}\sinh\tfrac{1}{2}\sqrt{\beta_l^2+\mathrm{i}\eta}\cosh\tfrac{1}{2}\beta_l-\beta_l\sinh\tfrac{1}{2}\beta_l\cosh\tfrac{1}{2}\sqrt{\beta_l^2+\mathrm{i}\eta}}. \tag{A 8}$$

The functions $p_m(y)$ and $q_l(x)$ satisfy boundary conditions

$$p_m\big(y=\pm\tfrac{1}{2}h\big)=1,\qquad \left.\frac{\mathrm{d}p_m}{\mathrm{d}y}\right|_{y=\pm h/2}=0, \tag{A 9}$$

$$q_l\big(x=\pm\tfrac{1}{2}\big)=1,\qquad \left.\frac{\mathrm{d}q_l}{\mathrm{d}x}\right|_{x=\pm 1/2}=0. \tag{A 10}$$

In this representation ξ satisfies the governing equation (A 3) inside the domain. Moreover, the first Fourier series in (A 6) can represent any even function corresponding to the boundary conditions imposed on ξ on the sides $|y|=h$ ($\xi(x,\pm h/2)=\mp h\mathscr{X}(x)/2$), and the second Fourier series can represent any even function corresponding to the boundary conditions imposed on ξ on the sides $|x|=1$ ($\xi(\pm 1/2,\,y)=\mp\mathscr{Y}(y)/2$). The boundary condition on the normal derivative $\partial\xi/\partial n=0$ on the sides is satisfied identically by the above choice of $p_m(y)$, $q_l(x)$ and α_m, β_l. Note that p_m and q_l decrease rapidly with distance from the boundary. Thus, the influence of the higher-order terms in (A 6) is confined to an increasingly narrow band along the boundary, so any small variation of the high-order coefficients has a negligible effect on the solution well inside the domain.

Imposing the remaining boundary conditions on ξ on the appropriate edges leads to

$$\xi_0 + h\sum_{m=1}^{\infty}(-1)^m \frac{X_m}{\alpha_m^2}\cos\alpha_m x + \sum_{l=1}^{\infty}\frac{Y_l}{\beta_l^2}q_l(x) = -\tfrac{1}{2}h\mathscr{X}(x), \tag{A 11}$$

$$\xi_0 + h\sum_{m=1}^{\infty}\frac{X_m}{\alpha_m^2}p_m(y) + \sum_{l=1}^{\infty}(-1)^l\frac{Y_l}{\beta_l^2}\cos\beta_l y = -\big(1-\tfrac{1}{2}h\big)\mathscr{Y}(y). \tag{A 12}$$

Standard Fourier inversion then yields an infinite system for the coefficients X_m and Y_l which can be written as

$$\left.\begin{aligned} X_m + \sum_{l=1}^{\infty} Y_l\,\hat{q}_{lm} &= \hat{\mathscr{X}}_m, \quad m = 1, 2, \ldots, \\ Y_l + \sum_{m=1}^{\infty} X_m\,\hat{p}_{ml} &= \hat{\mathscr{Y}}_l, \quad l = 1, 2, \ldots, \end{aligned}\right\} \tag{A 13}$$

and

$$\xi_0 = \hat{\mathscr{Y}}_0 - \sum_{m=1}^{\infty} X_m\,\hat{p}_{m0} = \hat{\mathscr{X}}_0 - \sum_{l=1}^{\infty} Y_l\,\hat{q}_{l0}, \tag{A 14}$$

where

$$\hat{p}_{m0} = \frac{2\,\mathrm{i}\eta}{\alpha_m^3\sqrt{\alpha_m^2+\mathrm{i}\eta}\big[\sqrt{\alpha_m^2+\mathrm{i}\eta}\coth\tfrac{1}{2}h\alpha_m - \alpha_m\coth\tfrac{1}{2}h\sqrt{\alpha_m^2+\mathrm{i}\eta}\big]}, \tag{A 15}$$

$$\hat{p}_{ml} = \frac{4\beta_l^2\mathrm{i}\eta\sqrt{\alpha_m^2+\mathrm{i}\eta}}{\alpha_m\big(\alpha_m^2+\beta_l^2\big)\big(\alpha_m^2+\beta_l^2+\mathrm{i}\eta\big)\big[\sqrt{\alpha_m^2+\mathrm{i}\eta}\coth\tfrac{1}{2}h\alpha_m - \alpha_m\coth\tfrac{1}{2}h\sqrt{\alpha_m^2+\mathrm{i}\eta}\big]}, \tag{A 16}$$

$$\hat{q}_{lm} = \frac{4\alpha_m^2\mathrm{i}\eta\sqrt{\beta_l^2+\mathrm{i}\eta}}{h\,\beta_l\big(\alpha_m^2+\beta_l^2\big)\big(\alpha_m^2+\beta_l^2+\mathrm{i}\eta\big)\big[\sqrt{\beta_l^2+\mathrm{i}\eta}\coth\tfrac{1}{2}\beta_l - \beta_l\coth\tfrac{1}{2}\sqrt{\beta_l^2+\mathrm{i}\eta}\big]}, \tag{A 17}$$

$$\hat{\mathscr{X}}_m = -\frac{\frac{1}{2}h\,2\mathrm{i}\eta}{h\big(\alpha_m^2+\mathrm{i}\eta\big)} \quad \text{for} \quad m = 1, 2, \ldots, \tag{A 18}$$

$$\hat{\mathscr{Y}}_0 = -\frac{1-\frac{1}{2}h}{12\mathrm{i}\eta}\big(6h\sqrt{\mathrm{i}\eta}\coth\tfrac{1}{2}h\sqrt{\mathrm{i}\eta} - h^2\mathrm{i}\eta - 12\big), \tag{A 19}$$

$$\hat{\mathscr{Y}}_l = \frac{\big(1-\frac{1}{2}h\big)\,2\mathrm{i}\eta}{\beta_l^2+\mathrm{i}\eta} \quad \text{for} \quad l = 1, 2, \ldots. \tag{A 20}$$

We now solve the system (A 13) by the standard method of reduction; we truncate the system (A 13) to M and L terms respectively and solve for coefficients X_m and Y_l. As shown by Kantorovich & Krylov (1958), as the level of truncation is increased, the solution converges to the true solution for 'fully regular' systems, i.e. (in this case)

$$\sum_{l=1}^{\infty}|\hat{q}_{lm}| \leqslant \delta < 1 \quad \text{for} \quad m = 1, 2, \ldots, \quad \sum_{m=1}^{\infty}|\hat{p}_{ml}| \leqslant \delta < 1 \quad \text{for} \quad l = 1, 2, \ldots, \tag{A 21}$$

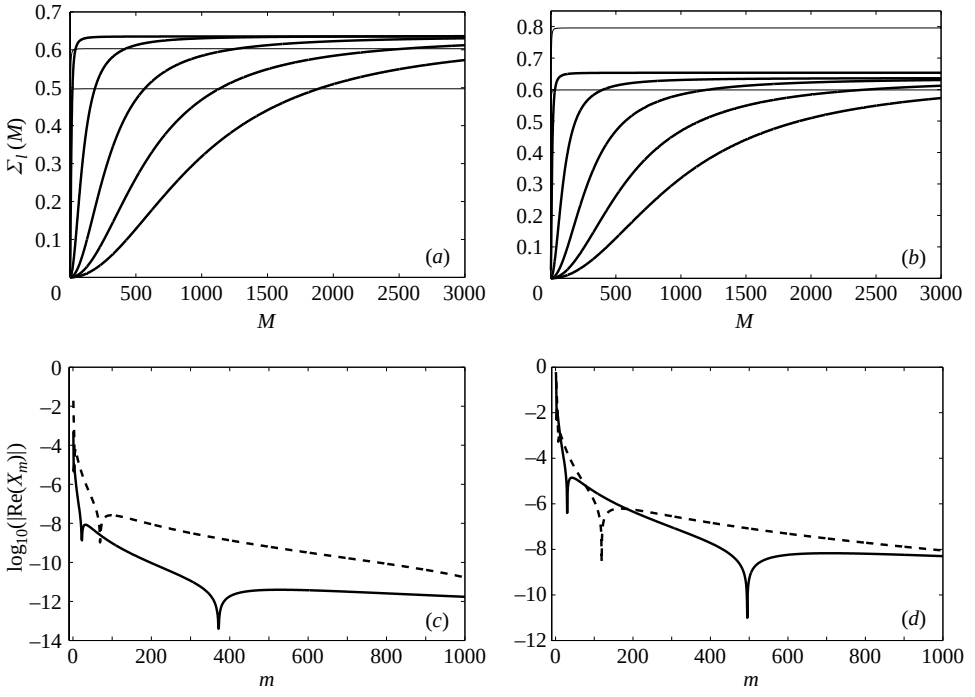

FIGURE 15. Oscillating-cylinder problem. (a, b) Numerically calculated partial sums $\Sigma_l(M)$ (A 22) for the case of square geometry $(h = 1;\ X_m = Y_m)$ and two different values of η: $(a)\ \eta = 1$, $(b)\ \eta = 100$; $l = 1, 2, 100, 300, 600, 1000$ in both cases. (c, d) First 1000 complex coefficients obtained by the method of reduction of the infinite system (A 13) for $(c)\ \eta = 1$ and $(d)\ \eta = 100$. In both cases the coefficients initially decrease rapidly with m. The decay becomes significantly slower with increasing m.

provided the positive constant δ exists and the free terms $\hat{\mathscr{X}}_m$, $\hat{\mathscr{Y}}_l$ in (A 13) are bounded. Moreover, increasing M and L does not significantly affect the coefficients with small indices.

Figure 15 provides strong evidence for the regularity of the system under consideration. It shows the behaviour of the partial sum

$$\Sigma_l(M) = \sum_{m=1}^{M} |\hat{p}_{ml}|, \tag{A 22}$$

for the case of a square domain, and it is evident that relations (A 21) are indeed satisfied in this case. Similar results (not presented here) have been obtained for a rectangular domain $(h \neq 1)$. We conjecture on the basis of these numerical results that the system (A 13) is indeed fully regular.

Figure 16 shows a comparison between the amplitude function $\hat{\psi}(x, y)$, given by (A 1), near a corner obtained for different number $(M + L)$ of the unknowns X_m, Y_l in the the truncated system (A 13) and the same amplitude calculated numerically using finite differences; results are presented for two values of η. The fourth-order finite-difference algorithm is similar to that described by Stephenson (1984) and uses a compact nine-point stencil that allows more accurate implementation of the no-slip boundary conditions. The accuracy of the semi-analytical method decreases with decreasing dimension of the truncated system but the location of the primary dividing

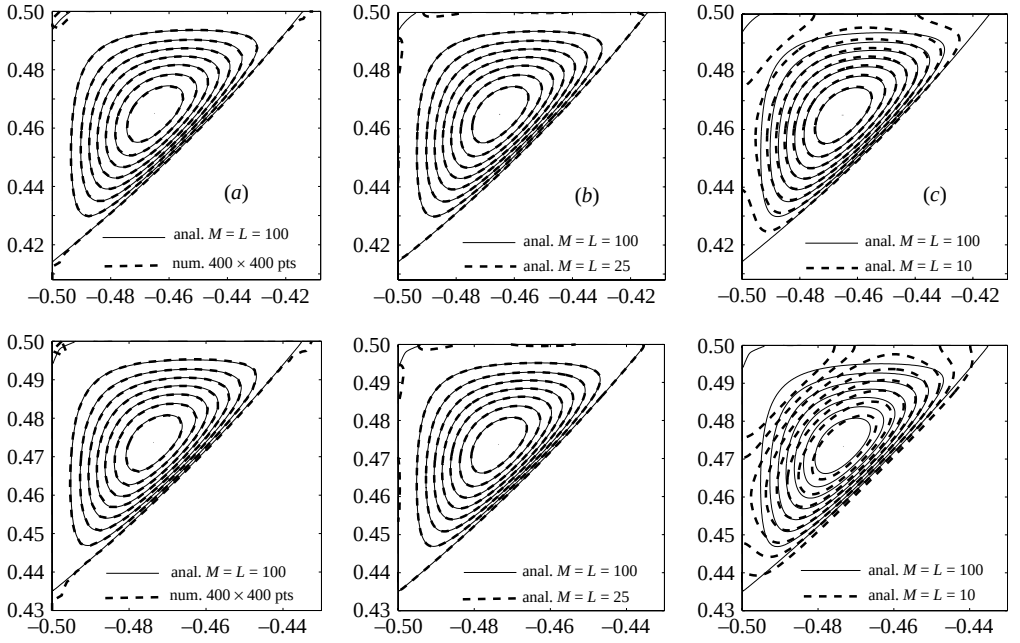

FIGURE 16. Comparison of two different techniques used to calculate the complex amplitude $\hat{\psi}$ in a square domain for the oscillating cylinder problem with: (*a–c*) $\eta = 1$, (*d–f*) $\eta = 100$. Results are shown for $\mathrm{Re}[\hat{\psi}]$ near one of the corners on the domain where the superposition method is least accurate. The numerical (fourth-order finite-difference) solution was computed on a 400×400 grid and the semi-analytical solution was obtained from the truncated system (A 13) for $M + L$ unknowns X_m and Y_l.

streamline is well-determined even for a relatively small number of terms used in the reduction method. In the interior, these two methods are in very good agreement even for a small number of terms used in the expansion (A 1).

The solution for $\hat{\psi}$ in the oscillating lid case ($\Lambda = 0$) can be obtained in a similar way and we do not present details of this procedure here. If the oscillating lid is located at $y = h/2$, the streamfunction has to be split into the sum

$$\hat{\psi} = \hat{\psi}_s(x, y) + \hat{\psi}_a(x, y) \tag{A 23}$$

of even ($\hat{\psi}_s$) and odd ($\hat{\psi}_a$) functions in y, and these two subproblems are then solved independently (due to the linearity of (2.9)). It can be checked numerically, as for the oscillating-cylinder problem (figure 15), that the two resulting infinite systems for the unknown coefficients are also fully regular in this case. However, convergence of the reduction method is much slower in this situation due to the discontinuity of the tangential velocity profile on the boundary.

The above treatment is sufficient for the purposes of investigating global characteristics of the flow reversal in a rectangle and is superior to the purely numerical finite-difference method in terms of both computational time and the insight provided into the structure of the solution. However, greater care is needed in order to accurately resolve the structure of the solution in the corners beyond the primary corner eddies. In particular, the possibility that the unknowns X_m, Y_l tend to some constant non-zero value would then require more careful consideration.

REFERENCES

Barenblatt, G. I. 1996 *Scaling, Self-Similarity, and Intermediate Asymptotics*. Cambridge University Press.

Goodier, J. N. 1934 An analogy between the slow motion of a viscous fluid in two dimensions, and systems of plane stress. *Phil. Mag.* (7) **17**, 554–576.

Kantorovich, L. V. & Krylov, V. I. 1958 *Approximate Methods of Higher Analysis*. Noordhoff Groningen.

Mathieu, E. 1881 Memoiré sur l'équilibre d'élasticité d'un prisme rectangle. *J. École Polytéchnique* **30**, 173–196.

Meleshko, V. V. 1996 Steady Stokes flow in a rectangular cavity. *Proc. R. Soc. Lond.* A **452**, 1999–2022.

Moffatt, H. K. 1964 Viscous and resistive eddies near a sharp corner. *J. Fluid Mech.* **18**, 1–18.

Moffatt, H. K. 1979 The asymptotic behaviour of solutions of the Navier-Stokes equations near sharp corners. In *Approximation Methods for Navier-Stokes Problems*. Lecture Notes in Mathematics, vol. 771 (ed. R. Rautman), pp. 371–380. Springer.

Moffatt, H. K. & Duffy, B. R. 1980 Local similarity solutions and their limitations. *J. Fluid Mech.* **96**, 299–313.

Shankar, P. N. 1993 The eddy structure in Stokes flow in a cavity. *J. Fluid Mech.* **250**, 371–383.

Shankar, P. N., Kidambi, R. & Hariharan, J. 2003 Oscillatory eddy structure in a container. *J. Fluid Mech.* **494**, 163–185.

Stephenson, J. W. 1984 Single cell discretisations of order two and four for biharmonic problems. *J. Comput. Phys.* **55**, 65–80.

Stokes, G. G. 1843 On some cases of fluid motion. *Trans. Camb. Phil. Soc.* VIII, 105 (Reprinted in *Mathematical and Physical Papers*, vol. I, pp. 17–68, Cambridge University Press, 1880).

Taylor, G. I. 1962 On scraping viscous fluid from a plane surface. (Reprinted in *Scientific Papers of G. I Taylor,* Vol. IV, pp. 410–413, Cambridge University Press, 1971.

Timoshenko, S. P. & Goodier, J. N. 1970 *Theory of Elasticity*, 3rd edn. McGraw-Hill.